~~Radiative Examination of Developing African Easterly Waves and~~ Saharan Dust ~~Interactions: Comparative Insights from~~ Impact on Radiative Heating Rate Errors Inherent in Reanalysis ~~and NASA Airborne Observations~~Data in African Easterly Wave Development Region

Ruby W. Burgess [1] and Mayra I. Oyola-Merced [1]

[1]University of Wisconsin-Madison, Madison, WI 53706, USA

Correspondence: Ruby W. Burgess (rwburgess@wisc.edu)

Abstract. This study thoroughly examines the impact of aerosols on atmospheric heating rates over the North Atlantic Ocean, with a specific focus on developing African Easterly Waves (AEWs). It utilizes data from the NASA DC-8 aircraft, dropsonde profiles, lidar observations, and satellite-based precipitation data obtained during NASA's CPEX-CV field campaign, as well as MERRA-2 and CAMS reanalyses. Using a four-stream radiative transfer model, the research focuses specifically on days characterized by Saharan dust coinciding with AEWs and tropical storm development and also contrasts its findings with a notable dust-only event in June 2020. The findings reveal notable differences in shortwave (SW) ~~and longwave~~heating rates of over 1.5 K/~~infrared (LW/IR) heating rates , underscoring~~ day between reanalysis and observations, underlining the persistent challenges in accurately representing aerosol effects in the atmosphere, even after assimilating observational data. These discrepancies ~~persisted~~ were present on days with both background and high dust concentrations, emphasizing the challenges in accurately representing aerosol radiative effects in models and highlighting the urgent need for improved aerosol representation in reanalysis datasets. A case study of two developing AEWs highlights a difference in heating rate on the order of 1 to 2 K/day between an AEW developing into a Category 4 Hurricane (Fiona) and a short-lived tropical storm (TS Hermine).

1 Introduction

Over the past two decades, substantial advancements have been made in characterizing aerosol properties, as well as in identifying their spatiotemporal distribution and their influence on the planet's radiative equilibrium (Ramanathan et al., 2001). This research has culminated in the recognition that aerosols have both a "direct effect" on climate by altering the Earth's radiative budget and redistributing heat throughout the atmosphere, as well as an "indirect effect" by impacting cloud formation, precipitation, and optical properties (IPCC, 2023). These effects are contingent on the concentration and altitude of aerosols (Lyapustin et al., 2011; Bauer and Menon, 2012; Xu et al., 2017). In the same period, significant strides have been made in aerosol modeling, data assimilation techniques for Numerical Weather Predictions (NWP) applications, and the development of precise 3-D aerosol models. These developments have enabled a more accurate representation of aerosols in weather mod-

els and reanalysis, leading to improvements in forecast accuracy (Mulcahy et al., 2014; Toll et al., 2016). Furthermore, these advancements have opened new avenues for advanced research on aerosol effects and provided the potential for monitoring air quality events. Nevertheless, uncertainties persist, especially concerning the atmosphere's response to various physical properties of aerosols, particularly on daily timescales that affect weather patterns (Mulcahy et al., 2014; Toll et al., 2016; Zhang et al., 2016). This is due to significant limitations in accurately characterizing aerosols, which are crucial for forecasting and understanding the evolution of weather systems and processes.

Aerosols, with characteristics such as concentration, size distribution, composition, vertical distribution, hygroscopicity, and mixing state, dynamically influence heating rates in the Earth's atmosphere. This influence stems from their complex ~~interplay,~~ role in orchestrating radiative processes within large-scale weather systems. For example, aerosol concentration significantly dictates the scattering and absorption of solar radiation, leading to regional variations in heating rates. Similarly, size distribution of aerosol particles governs their efficacy in scattering or absorbing radiation, impacting temperature gradients and atmospheric stability. Composition is pivotal, inducing localized atmospheric heating or cooling. Vertical distribution intricately shapes aerosol radiative effects across distinct atmospheric levels. Hygroscopic properties alter aerosol optical characteristics as they interact with water vapor, and mixing state complicates their radiative consequences. Therefore, understanding these aerosol-induced changes in heating rates is crucial for enhancing the accuracy of weather forecasting models and the reliability of reanalysis data. This knowledge enables a more precise representation of atmospheric processes and the development of weather systems.

The North Atlantic basin provides the setting for these processes to coexist. On a protagonist role are the African Easterly Waves (AEWs, Burpee, 1972; Reed et al., 1988; Thorncroft and Blackburn, 1999). Along with the African Easterly Jet (AEJ), they are the primary triggers of regional and synoptic weather events over the Atlantic basin (Reed et al., 1977), having devastating societal consequences over Africa, the Caribbean and the United States. Studies show, for example, that the AEJ-AEW system influences convection and rainfall over West Africa (Carlson, 1969; Reed et al., 1977), while more than half of the tropical cyclones that have been observed to develop over the eastern Atlantic Ocean have AEW origins (Landsea et al., 1998). Another important phenomenon is the Saharan dust (and associated Saharan Air Layer, SAL), a prominent aerosol feature that covers a vast portion of the Atlantic Ocean during boreal Spring and Summer (Carlson and Prospero, 1972; Dunion and Velden, 2004). The Saharan dust is believed to alter both short wave (SW) and longwave/infrared (LW/IR) solar radiation (Dunion and Velden, 2004) as well as temperatures at the surface and aloft (Nalli and Stowe, 2002; Oyola, 2015), decrease vertical wind shear, induce thermodynamic stability, and most notably, influence the genesis of tropical storms and hurricanes (Dunion and Velden, 2004; Pratt and Evans, 2009). Given that they share similarities in seasonality and geographical extent, the AEWs and Saharan dust are consequently coupled to influence each other. The United States Geostationary Operational Environmental Satellites (GOES) satellite imagery on Fig. 1 depicts an example of these interactions. On larger timescales, processes like the AEW trigger Saharan dust lofting by enhancing diurnal emission mechanisms (Dunion and Velden, 2004). On the other hand, dust atmospheric feedbacks influence the AEWs through direct and indirect radiative effects (Grogan and Thorncroft, 2019). We have advanced our understanding ~~on~~ of how Saharan dust affects AEW's structure and evolution, however, despite more than two decades of studies, no conclusive evidence has been agreed upon. From the observational/reanalysis stand-

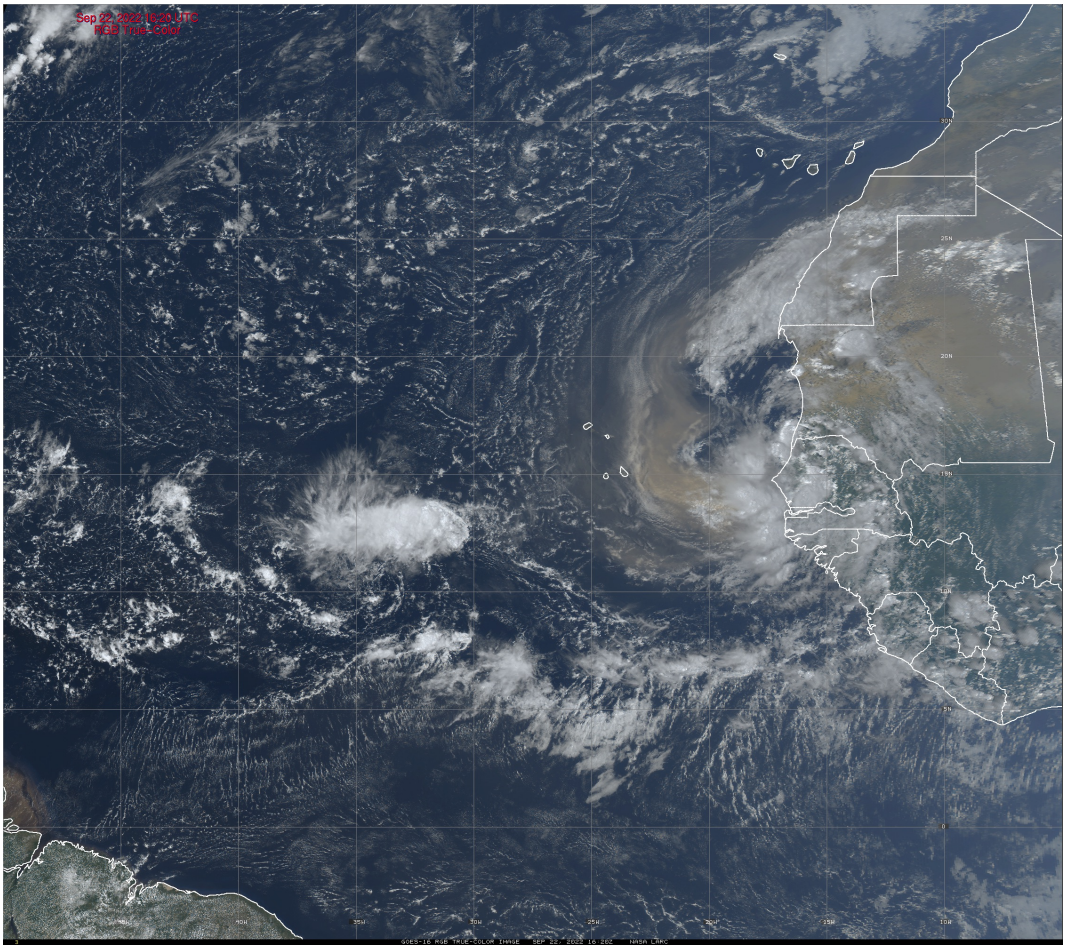

Figure 1. GOES-16 image of dust interacting with an African Easterly Wave on 22 September 2022 during the CPEX-CV field campaign (GOES-R Series Program, 2019).

point, most studies examining the effects of Saharan dust on AEWs using analytical approaches have produced contradictory results, and/or have only focused on attributing AEW growth or decay to dust-induced changes in the static stability alone (e.g. Karyampudi et al., 1999; Jones et al., 2004; Reale et al., 2009; Jury and Santiago, 2010; Reale et al., 2011; Ma et al., 2012). A significant limitation with these studies, and a possible reason behind their discrepancies, is that most focus on total column aerosol loading (or AOD) but have failed to properly address the relationship between the AEWs and changes in the vertical distribution of dust aerosols. Also, these studies do not directly address the dust impact at different stages of the AEW, nor clearly discretize changes in airmass in both systems with transatlantic passage. Although it seems a straightforward issue to address, previous research has been limited because retrieving good-quality measurements of vertical profiles of atmospheric parameters (moisture, wind, temperature, and vertical information of aerosols) in Saharan dust events remains an

extremely challenging endeavor, particularly in the lower atmosphere, as most of these techniques are biased due to changes in atmospheric composition itself (Nalli et al., 2011; Oyola, 2015).

There is an opportunity to characterize the impact of dust aerosols in AEWs, aiming to enhance our comprehension of their feedback mechanisms. This can be achieved by leveraging radiative transfer, aerosol vertical data from reanalysis, and, when accessible, utilizing existing field campaign datasets for atmospheric closure experiments. Obtaining high-resolution aerosol profiles from observations poses a significant challenge, particularly over oceanic regions, however, when such data is accessible, it can contribute significantly to addressing some of the questions that remain unanswered.

In this study, we shed light on the importance of accounting for the vertical distribution of Saharan dust in the context of AEW development by showing the impact of anomalous dust loadings on modifying atmospheric heating rates at critical atmospheric levels during AEW development. We show that these impacts are not well captured by reanalysis, a key factor in improving the modeling of AEW development. We integrate data collected during the airborne National Aeronautics and Space Administration (NASA) Convective Processes Experiment – Cabo Verde (CPEX-CV) and profiles from two different global reanalyses into a four-stream radiative transfer model. ~~Our primary objective is to perform a radiative examination of the interactions between AEWs and Saharan Dust~~ We examine radiative heating rates within Saharan dust plumes associated with AEWs during the intensive observation period (IOP). The CPEX-CV datasets provide a distinctive opportunity for this model evaluation, featuring collocated aircraft instrumentation that simultaneously measured high-resolution vertical aerosol profiles ~~with~~ and atmospheric profiles via dropsondes over AEWs. Utilizing this in situ instrumentation, our goal is to assess the reanalyses' accuracy in depicting aerosol radiative properties. Specifically, within the observational constraints of the limited dataset available for this study, our objectives include ~~understanding~~ quantifying the magnitude of ~~aerosol~~ aerosol-induced heating rates—particularly those associated with ~~dust~~high dust loading—and ~~considering their potential influence on AEW development and model representation~~ shedding light on their potential to influence model representation of AEW development.

2 Data and methods

The analysis was conducted over the North Atlantic Ocean, in a box spanning 0°to 25°N and 15°W to 35°W to the west of the Sahara Desert. Data from several reanalyses and the CPEX-CV field campaign were used to analyze the effects of aerosols on atmospheric profiles and their ~~impact on~~ role in the development of AEWs.

2.1 CPEX-CV

CPEX-CV was conducted between 1 and 30 September 2022 out of Cabo Verde over the North Atlantic. Its objectives included examining the interplay of atmospheric dynamics, properties of the marine boundary layer, convection, the Saharan Air Layer and Saharan dust, and their interactions at different spatial scales. The mission aimed to enhance our comprehension and predictive capabilities regarding the lifecycles of processes such as AEWs, aiming to increase our understanding of such processes in a data-scarce region such as the tropical East Atlantic. During the field campaign, data were collected during

fourteen research flights from the NASA DC-8 aircraft by several instruments including the ones described below. We make use of data from the seven research flights that coincided with a developing AEW.

2.1.1 AVAPS dropsondes

The Advanced Vertical Atmospheric Profiling System or AVAPS (Hock, 1999), is a dropsonde system providing vertical profiles of pressure, temperature, specific humidity, and winds that was used onboard the DC-8 during CPEX-CV. Dropsondes were launched at multiple locations during each flight. The profile altitude was limited to the DC-8 aircraft's maximum altitude of 42,000 ft, and most profiles did not contain data above 200 hPa. We employ 64 dropsonde profiles of pressure, temperature, and specific humidity throughout seven research flights to characterize atmospheric conditions in our analysis. We use mean daily profiles of pressure, temperature, and specific humidity from the AVAPS dropsonde dataset to calculate mean heating rates for two days of interest (09 and 22 September).

2.1.2 HALO

The NASA Langley High Altitude Lidar Observatory or HALO (Bedka et al., 2021) is a lidar system operated from an airborne platform to provide nadir-viewing profiles of water vapor, methane columns, and profiles of aerosol and cloud optical properties. The HALO profiled the vertical distribution of aerosol in the atmosphere during each of the research flights used in our analysis. ~~We utilize the~~ The 532 nm aerosol extinction coefficient, inferred from the aerosol backscatter (Carroll et al., 2022; Lei et al., 2022; Lenhardt et al., 2022) is used in our experiments as a measure of extinction coefficient. ~~We use mean daily profiles of pressure, temperature, and specific humidity from HALO to calculate mean heating rates for two days of interest (09 and 22 September).~~ The latitude and longitude data from ~~this~~ the HALO dataset were used to determine the flight track location for each flight used in the analysis.

2.2 MERRA-2

The Modern-Era Retrospective Analysis for Research and Applications, Version 2 (MERRA-2, Buchard et al., 2017; Gelaro et al., 2017; Randles et al., 2017) is a reanalysis dataset developed by NASA that provides comprehensive and high-quality atmospheric data from 1980 onward, including the assimilation of aerosols and a representation of their interactions with other physical processes. We utilize the 3D 6-hourly Analyzed Meteorological Fields dataset (or inst6_3d_ana_Nv on 72 levels) for profiles of pressure, temperature, specific humidity, and ozone mixing ratio. For aerosol, we utilize the inst3_3d_aer_Nv collection, which includes instantaneous 3-dimensional 3-hourly data within MERRA-2. This dataset encompasses assimilated aerosol mixing ratio parameters at 72 model layers, including dust, sulfur dioxide, sea salt, black carbon, and organic carbon. Similarly, we also obtain 3-hourly Aerosol Optical Depth (AOD) Analysis from the inst3_2d_gas_Nx.

~~An additional~~ Additional treatment is required to be able to obtain extinction coefficient profiles from dust concentration. We calculate ~~extinction coefficient from each dust mixing ratio profile bin concentration profile~~ volume extinction coefficient at each level from dust mixing ratio for each of the five ~~bins~~ size-bins provided in the aerosol mixing ratio dataset, using the

following equation:

$$\beta_e = k_e \rho_{air} = \frac{3 R_{DU} Q_{ext}}{4 r \rho_p} \rho_{air} \quad (1)$$

where k_e is the mass extinction coefficient in m^2 kg^{-1}, ρ_{air} is the air density in kg m^{-3}, R_{DU} is the dust mass mixing ratio for a specific bin in kg kg^{-1}, Q_{ext} is the extinction efficiency, r is the particle radius in m, and ρ_p is the particle density in kg m^{-3}. The air density was provided by the MERRA-2 analyzed meteorological fields. The particle radius used for each of the five ~~bins~~ size-bins is 0.73 μm, 1.4 μm, 2.4 μm, 4.5 μm, 8.0 μm respectively. The particle density is 2500 kg m^{-3} for particles of mean radius of 0.73 μm, and 2650 kg m^{-3} for the rest of the ~~bins~~ size-bins (GMAO, 2023). The extinction efficiency was approximated for each ~~bin~~ size-bin using values from the Goddard Chemistry Aerosol Radiation and Transport (GOCART) module GMAO (2023) that correspond to the closest particle radius for each bin. The HALO data collected during the CPEX-CV campaign were assimilated into the MERRA-2 reanalysis (Nowottnick et al., 2023), and our analysis ~~examines~~ sheds light on the performance of the assimilation.

2.3 CAMS

~~It is noteworthy to mention that~~ Because the CPEX-CV data were assimilated into the MERRA-2 reanalysis dataset used in this study~~. We~~, we use the Copernicus Atmosphere Monitoring Service reanalysis (CAMS, Inness et al., 2019), which did not assimilate data from CPEX-CV, as a reference to assess the impacts of assimilation on the reanalysis. CAMS is a reanalysis dataset that comprises 3D time-consistent atmospheric composition fields, including aerosols, chemical species, and greenhouse gases. We utilize the 3-hourly datasets on 25 pressure levels for temperature, specific humidity, and dust aerosol mixing ratio at three different particle size ranges (0.03 - 0.55 μm, 0.55 - 0.9 μm, 0.9 - 20 μm), as well as the total column AOD at 550 nm. Similar to the MERRA-2 dataset, we calculate the extinction coefficient at each level for the 3 dust ~~bins~~ size-bins listed above using the following formula:

$$\beta_e = k_e \rho_{air} = \frac{3 R_{DU} Q_{ext}}{4 r \rho_p} \cdot \frac{p}{R_d T_v} \quad (2)$$

where $T_v = (1 + 0.61q)T$ and p is the pressure in hPa, R_d is the gas constant for dry air in J kg^{-1} K^{-1}, T_v is the virtual temperature in K, q is the specific humidity in kg kg^{-1}, and T is the temperature in K. The pressure, specific humidity, and temperature were provided by the CAMS dataset. Since CAMS also uses GOCART aerosol properties, the values for extinction efficiency, particle radius, and particle density for each of the three ~~bins~~ size-bins are the same used for MERRA-2 for particle radii sizes of 0.24 μm, 0.8 μm, and 8 μm respectively. ~~Similar~~ Similarly to the MERRA-2 dataset, the values for extinction coefficient were added together to calculate the total dust aerosol extinction coefficient. Because each ~~bin~~ size-bin represents a range of particle sizes and the extinction efficiency depends on particle size, the accuracy of the extinction coefficient remains limited for both the MERRA-2 and CAMS datasets.

2.4 ~~IMERG~~AEW Tracking

The Integrated Multi-satellitE Retrievals for Global Precipitation Measurement (IMERG, Huffman et al., 2020) is a dataset developed and provided by NASA that offers global precipitation data by merging and integrating data from the Global Precipitation Measurement (GPM) satellite constellation. We leverage the daily mean data within the IMERG dataset to identify and ~~track the~~ follow the progression of the sampled AEWs within our designated geographic region. To delve deeper into the dust-AEW intricate interplay, we superimpose IMERG data with the MERRA-2 total dust mixing ratio dataset as in Fig. 2. This integrated approach allows us to explore how and where dust aerosols may be influencing AEW dynamics, providing a more comprehensive view of the factors affecting AEW behavior.

We use the AEW tracker described in Lawton et al. (2022) to track the center of several AEWs of interest. The tracker calculates curvature vorticity at 700 hPa using the nondivergent component of the 700-hPa wind averaged within a radius of 600 km of each grid point. We use the positional dataset which supplies an approximation of the location of the center of the storm at a 6-hour time step to collocate the center of the storm with the nearest MERRA-2 and CAMS reanalysis datasets./

2.5 Data processing

2.5.1 Observational analysis

The MERRA-2 total dust ~~concentration~~ mixing ratio was derived by aggregating the contributions from five distinct ~~dust mixing ratio bins~~particle size-bins. To explore the dynamics of dust in relation to convection and precipitation, we superimposed MERRA-2 total dust mixing ratio onto IMERG daily accumulated precipitation, enabling the creation of daily maps (e.g. Fig. 2). These maps provided valuable insights into the interplay between dust and AEWs. In the process of our analysis, we leveraged these maps, in conjunction with the daily forecast reports from CPEX-CV to identify specific days of interest. Furthermore, we utilized these maps to track the temporal evolution of dust concentration throughout the field campaign. Additionally, we assessed the integration of CPEX-CV data into the MERRA-2 reanalysis, examining how this assimilation impacted the overall dataset.

2.5.2 Data processing for radiative transfer

We use the positional data from the CPEX-CV HALO dataset to collocate data from the two reanalyses (MERRA-2 and CAMS) with the CPEX-CV dataset. We process the AVAPS dropsonde data to select profiles of pressure, temperature, and specific humidity with sufficient information to be run in the Fu-Liou-Gu (FLG) radiative transfer model (RTM) (Gu et al., 2011). We generate profiles from MERRA-2 and CAMS reanalysis at the ~~same~~ each dropsonde profile location. Similarly, we process extinction coefficient profiles from HALO to select profiles providing sufficient aerosol extinction ~~information~~coefficient data. We select extinction coefficient profiles from the HALO, MERRA-2, and CAMS datasets matching the location of the selected dropsonde profiles~~, and interpolate these~~. We interpolate all profiles to 72 vertical levels, restricting ~~the~~ both the atmospheric and extinction coefficient profiles to below the 100 hPa level. ~~We~~ Values of AOD are retrieved for each location using the

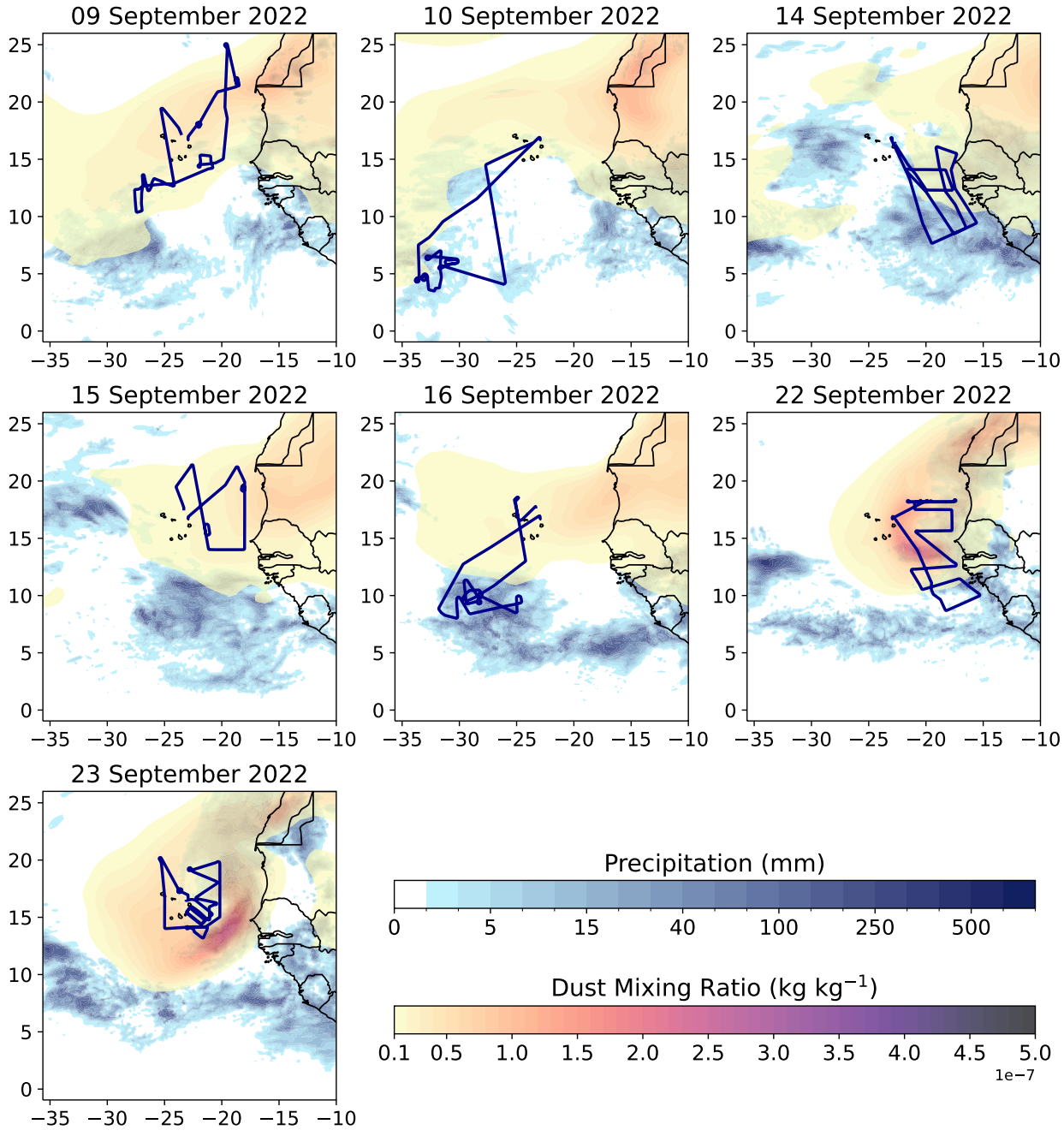

Figure 2. Flight tracks (blue) with overlaid total dust mixing ratio from MERRA-2 and daily accumulated precipitation from IMERG for seven of the research flights during the CPEX-CV field campaign.

Table 1. FLG Input parameter datasets for PTQ (atmospheric profile of pressure, temperature, and humidity) and extinction coefficient (see text for further details on parameter calculations).

Dataset	PTQ	Extincti
CPEX-CV ~~, Aerosol Optical Depth Analysis from~~	AVAPS Dropsondes	HALO Extin
MERRA-2 ~~and Total Aerosol Optical Depth at 550 nm from CAMS.~~	6-hourly Analyzed Meteorological Fields	Extinction coefficient fro
CAMS	3-hourly pressure, temperature, specific humidity	Extinction coefficient fro

532 nm Total Optical Thickness from CPEX-CV, Aerosol Optical Depth Analysis from MERRA-2 and Total Aerosol Optical Depth at 550 nm from CAMS. These profiles, along with AOD values, are used for the calculation of heating rates using the FLG RTM. A summary of datasets used as inputs in the FLG RTM is given in Table 1. For our AEW case study, we calculate a mean pressure, temperature ~~, specific humidity and extinction~~ and specific humidity profile from the AVAPS dropsonde dataset and a mean extinction coefficient profile from the HALO extinction coefficient dataset for each flight~~as well as corresponding profiles~~. We generate a corresponding mean atmospheric profile and extinction coefficient profile from both reanalyses ~~. These profiles, which are interpolated to 72 levels, are used to analyze~~ using a collocated dataset. These mean profiles are used in the case study of daily mean heating rates during the AEW events on 09 September and 22 September. ~~Values of AOD were retrieved for each location using the 532 nm Total Optical Thickness from~~ We also use the AEW tracking methodology described in section 2.4 to generate heating rate profiles at 6-hour time steps during the development of the AEWs studied.

2.6 Fu-Liou-Gu Radiative Transfer Model~~(FLG RTM)~~

The Fu-Liou-Gu ~~(FLG) radiative transfer (RT) model is used to calculate~~ RT model calculates heating rates and irradiances (fluxes) from ~~the different~~ profiles generated from the datasets described above. The FLG RT scheme, as proposed by Gu et al. (2011), represents an upgraded iteration of FLG originally developed by Fu and Liou in 1992 and ~~1993.~~ 1993 (Fu and Liou, 1992, 1993). This refined model offers improved parameterizations for aerosol properties, which enable more accurate simulation of radiative effects, aligning more closely to real-world observations. The delta-four-stream approximation is utilized for solar radiative flux calculations (Liou et al., 1988) and the delta-two-and-four-stream approximation is employed for LW/IR radiative flux calculations (Fu et al., 1997) in the model. The model divides the solar and LW/IR spectra into 6 and 12 bands respectively, determined by the locations of absorption bands, and the calculations incorporate the effect of absorption by the H2O continuum and various minor absorbers within the solar spectrum in addition to the principal absorbing gases.

2.6.1 OPAC

The current FLG radiation scheme contains a total of 18 aerosol types parametrized by the Optical Properties of Aerosols and Clouds (OPAC, Hess et al., 1998) database. This database provides humidity-aware single-scattering properties for spherical aerosols computed from Lorenz Mie theory, for 60 wavelengths in the spectral region between 0.3 μm and 40 μm. These

60 bands are interpolated into the 18 bands of the FLG RT scheme. The 18 types of aerosol include maritime, continental, urban, five ~~size bins~~ size-bins for mineral dust, insoluble, water soluble, soot (BC), sulfate droplets, sea salt in two modes (accumulation and coarse mode), and mineral dust in four different modes (nucleation, accumulation, coarse, and transported mode). For the purposes of this study, we employ the mineral dust transported mode.

2.6.2 Calculation of heating rates

Following a similar approach to (Oyola et al., 2019), we run the ~~model~~ FLG RTM ingesting atmospheric profiles from the three datasets (MERRA-2, CAMS, and CPEX-CV) to retrieve heating rates throughout the vertical layer at each of the selected dropsonde locations. Simulations are performed after ~~taking~~ accounting for the solar zenith angle at the corresponding local time and location~~into consideration~~. The heating rates are given by (e.g. Petty, 2008):

$$\mathcal{H}(z) \equiv -\frac{1}{\rho(z)C_p}\Bigg\{-[F_i^{\uparrow}(0)-\Delta\tilde{v}_l\pi\bar{B}_l(z)]\frac{\partial\tau_i(0,z)}{\partial z} - [F_i^{\downarrow}(\infty)-\Delta\tilde{v}_l\pi\bar{B}_l(z)]\frac{\partial\tau_i(z,\infty)}{\partial z} - \Delta\tilde{v}_l\pi\int_z^{\infty}[\bar{B}_l(z')-\bar{B}_l(z)]\frac{\partial^2\tau_i(z,z')}{\partial z'dz}dz' - \Delta\tilde{v}_l\pi\int_0^{z}[\bar{B}_l(z')-\bar{B}_l(z)]\frac{\partial^2\tau_i(z',z)}{\partial z'dz}dz'\Bigg\} \quad (3)$$

where $\rho(z)$ is the air density at level z, C_p= 1005 J kg^{-1} K^{-1} is the specific heat capacity of air at constant pressure, τ_i is the band average flux transmittance, $\tilde{v}_l$ represents the spectral interval or band (SW, LW/IR), $F_i^{\uparrow}$, $F_i^{\downarrow}$, $F_i^{\uparrow}(0)$, $F_i^{\downarrow}(\infty)$ are fluxes where the arrows represent the direction of incoming flow (from surface up from top of atmosphere to surface), and the indices 0 and ∞ represent the surface and TOA respectively. The heating rate is dominated in magnitude by the first two terms: the first term quantifies radiative exchange with the boundary layer and is generally a heating term, while the second term quantifies radiative exchange with the top of the atmosphere and thus predicts longwave/infrared cooling to space. In its summarized form, the heating rate equation can be stated as:

$$\mathcal{H}(z) \equiv -\frac{1}{\rho(z)C_p}\frac{\partial F_{net}}{\partial z} \quad (4)$$

Here, F_{net} is the net flux given by the difference between upward and ~~downward directed~~ downward-directed fluxes. We set a control RTM run for each profile where no aerosol feedback is included~~and a parallel~~, which we run parallel to the RTM run using the extinction coefficient profiles calculated from each of the three respective datasets ~~,~~ for each of the profile locations.

2.6.3 ~~Categorization of background and anomalous AOD cases~~Heating rate experiments

We distinguish between background AOD and anomalous AOD to emphasize the impact of dust concentration on atmospheric heating rates. We define a threshold of AOD < 0.2 (which is considered a background AOD level) calculated from the CPEX-CV 532 nm total optical thickness to select background dust concentration profiles. We obtain 32 dropsonde locations which

Table 2. Mean AOD for background and anomalous cases over the seven research flights for CPEX-CV, MERRA-2 and CAMS.

Dataset	Mean Background AOD	Mean Anomalous AOD
CPEX-CV	0.09	0.83
MERRA-2	0.22	0.46
CAMS	0.27	0.33

fit the condition of background AOD (AOD < 0.2), and we select profiles from all three datasets at these locations. We then select the top 32 dropsonde locations with highest AOD calculated from CPEX-CV 532 nm total optical thickness and define these as anomalous dust concentration profiles, and select profiles from all three datasets at these locations. The resulting mean AOD value for the background and anomalous cases for each dataset are shown in Table ~~1.~~ 2. The profiles selected for the background and anomalous cases for MERRA-2 and CAMS are based on the CPEX-CV AOD threshold, not MERRA-2 and CAMS AOD values, and thus have a differing range of AOD values. The 64 dropsonde profiles of temperature, specific humidity, and extinction coefficient are ingested into the FLG RTM, which is run for all three datasets (CPEX-CV, MERRA-2, and CAMS) at each dropsonde location at the time of launch. We refer to these runs as the aerosol-aware case. A control run where the aerosol parameter was turned off ~~was~~ is also performed for each run. The mean shortwave (SW), longwave/infrared (LW/IR), and total heating rate differences between the aerosol runs and the control runs are calculated using the FLG RTM. The results are plotted for background dust concentration profiles in Fig. 4 and for anomalous dust concentration profiles in Fig. 5.

3 Results and discussion

3.1 Description of AEW events during CPEX-CV

In our analysis, we focused on data collected within a region defined by latitudes ranging from 0° to 25° N and longitudes from 15° to 35° W. During the CPEX-CV field campaign, the fourteen DC-8 research flights sampled 10 different African Easterly Waves (AEWs) identified as AEW 1 through AEW 10. Four of these waves developed into named tropical storms (AEW 4, 5, 6, 8), with two intensifying into hurricanes (AEW 4, 6). For this study, we utilized profiles collocated with dropsondes obtained during developing AEW events, which correspond to the flights on 9, 10, 14, 15, 16, 22, and 23 September, resulting in 64 profiles over 4 AEWs or their surrounding environments. Table ~~1~~ 3 provides specific information about ~~these developing AEWs~~ the developing AEWs corresponding to the research flights. Environmental conditions varied for each flight, as illustrated in Fig. 2, which displays flight tracks for several days of interest and corresponding weather conditions. Integrated dust concentration from MERRA-2 and accumulated IR-MW precipitation from IMERG highlight different regimes sampled, such as conditions where mainly dust is present (09 and 15 September), conditions where the "dusty" outer environment relative to the AEW was sampled (14 September), and situations where AEWs interacted with heavy dust loadings (22-23 September).

Table 3. Flight date, time, location, mean and maximum AOD, location relative to AEW and corresponding tropical cyclone for seven days corresponding to a developing AEW.

Flight Date	Flight times	Location	Mean AOD	Max AOD	Location Relative to AEW	Corresponding TC
09 September	12:06:35 to 20:40:03 UTC	10.4°– 25.1°N, 18.5°W – 27.6°W	0.25	1.69	In AEW 4 region	Fiona
10 September	13:42:27 to 21:19:37 UTC	3.5°– 16.9°N, 22.9°W – 33.8°W	0.07	0.26	In AEW 4 region	Fiona
14 September	09:03:44 to 16:27:09 UTC	7.7°– 16.9°N, 15.6°W – 23.0°W	0.06	1.02	Between AEW 5 and AEW 6	Gaston and Ian
15 September	15:04:47 to 20:26:22 UTC	14.0°– 21.4°N, 18.0°W – 24.0°W	0.36	1.10	North of AEW 6	Ian
16 September	12:52:20 to 20:26:15 UTC	8.0°– 18.6°N, 22.9°W – 31.8°W	0.23	1.14	In AEW 6 region	Ian
22 September	04:53:21 to 12:36:42 UTC	8.7°– 18.4°N, 15.3°W – 23.0°W	1.02	3.34	In AEW 8 region	Hermine
23 September	06:48:29 to 14:17:34 UTC	13.2°– 20.2°N, 20.2°W – 25.5°W	0.52	1.51	In AEW 8 region	Hermine

On 09 September, AEW 4 was located off the west coast of Africa, later evolving into Tropical Storm Fiona on 14 September and further intensifying into a hurricane on 18 September. Fiona reached Category 4 with the highest 1-minute sustained winds of 140 mph (220 km/h) and produced catastrophic damage to many islands in the Caribbean. On 23 September, it transitioned into an ~~Extratropical Cyclone~~extra-tropical cyclone, directly impacting the Atlantic portion of Canada and becoming the costliest cyclone in Canadian history. It finally dissipated on 27 September 2022. The DC-8 aircraft sampled the early stages of this storm on 09 September (first panel, Fig. 2), and the resulting data are analyzed in our study.

AEW 5 moved off the west coast of Africa on 12 September, initially producing disorganized showers and thunderstorms, but eventually developing into Tropical Storm Gaston on 20 September. Gaston dissipated by 25 September when additional strengthening was prevented by colder and drier air intrusion. Between 14 and 15 September, AEW 6 moved off the west coast, transforming into Tropical Storm Ian on 24 September and intensifying into a hurricane on 26 September. The research flight on 14 September flew between AEW 5 (TS Gaston, ~~second~~ third Panel Fig. 2) and AEW 6 (Hurricane Ian, ~~second~~ third Panel Fig. 2), while the flight on 15 September traversed north of AEW 6, sampling a dust storm located in the outer storm environment of the AEW (~~third~~ fourth Panel Fig. 2).

On 22 September, AEW 8 moved off the African coast, transforming into Tropical Storm Hermine on 23 September before weakening back to a tropical depression on 24 September. This storm, coinciding with the highest concentrations of Saharan dust sampled during the CPEX-CV field campaign, was studied on ~~22nd and 23rd September ,~~ 22 and 23 September (sixth and seventh panel, Fig. 2), and the resulting data are included in our analysis~~(fourth and fifth panel, Fig. 2).~~ . Additional detailed information on developing AEWs is provided in Table ~~2.~~ 3.

3.2 Impact of aerosol on heating rates

Profiles of mean temperature in Kelvin (top row), specific humidity in kg/kg (middle row), and aerosol extinction coefficient in km^{-1} (bottom row) which were utilized in the radiative transfer calculation are depicted in Fig. 3. The grey shading shows the spread of all profiles ~~used~~ ingested in the RTM, for both background and anomalous aerosol concentrations. CPEX-CV data (considered as the truth) is shown in the left column ~~,~~ (where temperature and humidity data are from the AVAPS dropsonde dataset, and extinction coefficient data from the HALO dataset), while the other two columns show the collocated mean profiles and corresponding spread obtained from MERRA-2 and CAMS reanalysis. The temperature and moisture profiles across the three datasets exhibit striking similarities. ~~The~~ However, the specific humidity profiles exhibit high variability ~~in all~~ across the three datasets (CPEX-CV, MERRA-2, and CAMS), ~~reflected in larger spread for all three datasets. This points to a broader and more diverse distribution of specific humidity values, particularly noticeable in the region~~ as seen from the large spread of profiles specifically between the surface and 800 hPa. This variability impacts heating rate profiles, which is especially noticeable at these levels for heating rates calculated from the CAMS dataset.

On the other hand, comparisons reveal significant disparities when examining aerosol extinction coefficient profiles. At this point, it is noteworthy to remind the reader that MERRA-2 assimilated data collected during CPEX-CV. Despite the assimilation of CPEX-CV data into MERRA-2, MERRA extinction coefficient profiles exhibit much higher surface extinction coefficient compared to the CPEX-CV data ~~(particularly~~ in the atmospheric layer between 1000 – 900 hPa)~~, however, missing~~

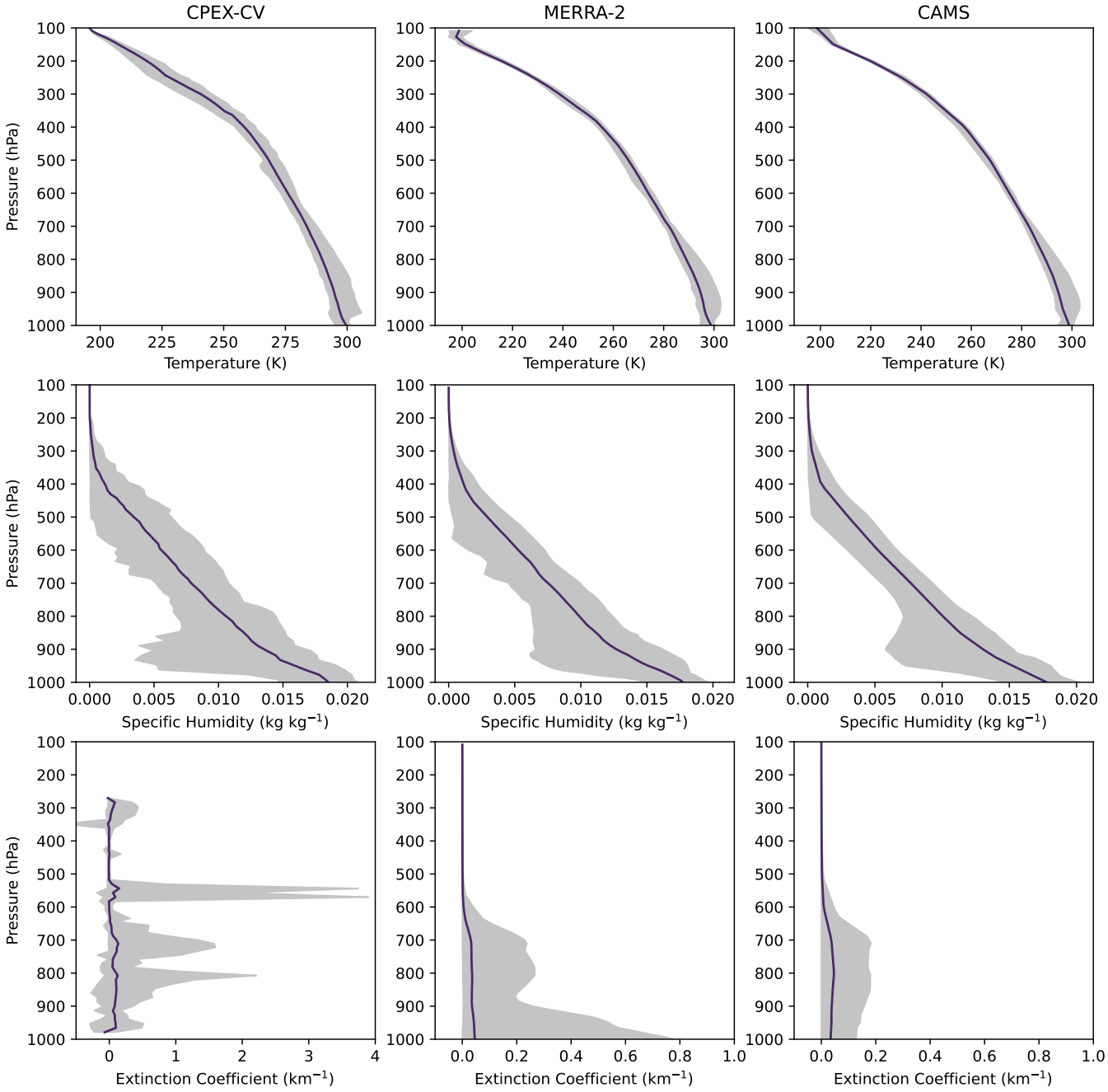

Figure 3. Temperature, specific humidity and extinction coefficient mean (magenta) and range (grey shading) for all CPEX-CV, MERRA-2 and CAMS profiles used in the study, including background and anomalous dust concentrations (note the difference in the x-axis scale between the leftmost extinction coefficient panel and the center and rightmost panels).

. However, both MERRA-2 and CPEX-CV miss most of the variability in extinction coefficient throughout the tropospheric column that the HALO profiles ~~were able to~~ capture, including several notable aerosol layers around 800, 700, and ~~650~~ 550 hPa. In the case of MERRA-2, most of the aerosol is confined to the first 600 hPa. The contrast becomes even more pronounced when comparing the CPEX-CV and MERRA-2 against CAMS extinction coefficient. CAMS underestimates the extinction coefficient by an order of magnitude in several portions of the troposphere. Interestingly enough, the differences found for aerosol loading are not only confined to the extinction coefficient profiles, but there are also noticeable differences in AOD. The mean AOD for background and anomalous cases over the seven research flights for CPEX-CV, MERRA-2, and CAMS are summarized in Table ~~1.~~ 2. There are significant differences in the mean observed AODs and the ones provided by the reanalysis. ~~It seems~~ In general, the reanalysis overestimates the AOD compared to the observations for background cases and underestimates it for the anomalous cases. These differences ~~will~~ result in significant discrepancies in the heating rate calculations, as we will discuss below.

As mentioned ~~before~~above, 64 different cases were identified, all within a developing AEW or its environment. ~~Each~~ For each one of these cases~~use~~ , we run the RTM for 3 datasets (CPEX-CV, MERRA-2, and CAMS), and for each of them, two RTM runs are performed: one without the aerosol effect (RTM only initialized with pressure, temperature, specific humidity, and ozone), which we refer to as the control run, and another one ~~with all of~~ using the same atmospheric information ~~and also aerosol extinction~~ with an added aerosol extinction coefficient profile and corresponding AOD, which we refer to as the aerosol-aware run, for a total of 384 runs. Fluxes (in W/m^2) and heating rates (in K/day) are thus calculated for each one of the 384 cases. To better understand the impact of different dust loading scenarios, we categorize the data into two groups based on ~~dust~~ AOD as sampled during CPEX-CV. We thus ~~defined~~ define as background all profiles with AOD ≤ 0.2 and select an equal number of profiles (32 profiles) with the highest AOD which ~~are defined~~ we define as "anomalous" or high (~~lowest~~ where the minimum AOD that meets this criteria is 0.335). This approach resulted in a 50-50 data split; in other words, 50% of the profiles are labeled as anomalous or high dust, while the lower 50% was classified as low or background dust.

We ~~then proceeded~~ proceed to subtract the ~~aerosol-aware~~ control run from the ~~control run for each case to its corresponding dataset to~~ aerosol-aware run at each profile location to evaluate the impacts of dust on heating rates. We ~~calculated~~ calculate the mean and corresponding standard deviations for our aerosol-aware minus control profiles. Figure 4 shows the mean heating ~~rates~~ rate differences (aerosol-aware minus control) for low~~or background dust~~ /background dust concentration and Fig. 5 shows the same for anomalous dust concentrations. Heating rate differentials are provided in three panels: shortwave (SW), longwave/infrared (LW/IR), and total heating rate differences between the aerosol-aware run and the control run.

Figure 4 reveals notable discrepancies between datasets in the calculated heating ~~rates~~ rate differences, particularly in the SW contribution. The differences in SW heating rate profiles, especially the significant divergence below 800 hPa, can be attributed to variations in distribution (as indicated by extinction coefficient profiles), specifically the differences in AOD detailed in Table 2. CAMS reports the highest mean AOD for the background cases, and this is reflected in both the vertical distribution and magnitude of heating rates, particularly below 900 hPa. Both reanalysis profiles exhibit significantly higher SW heating rates near the surface, exceeding 1 K, while the CPEX-CV profiles maintain a more modest ~~increase~~difference, not exceeding 0.4 K ~~in the same region. Interestingly, most~~ at the surface. Most of the contribution to total heating rates comes from SW

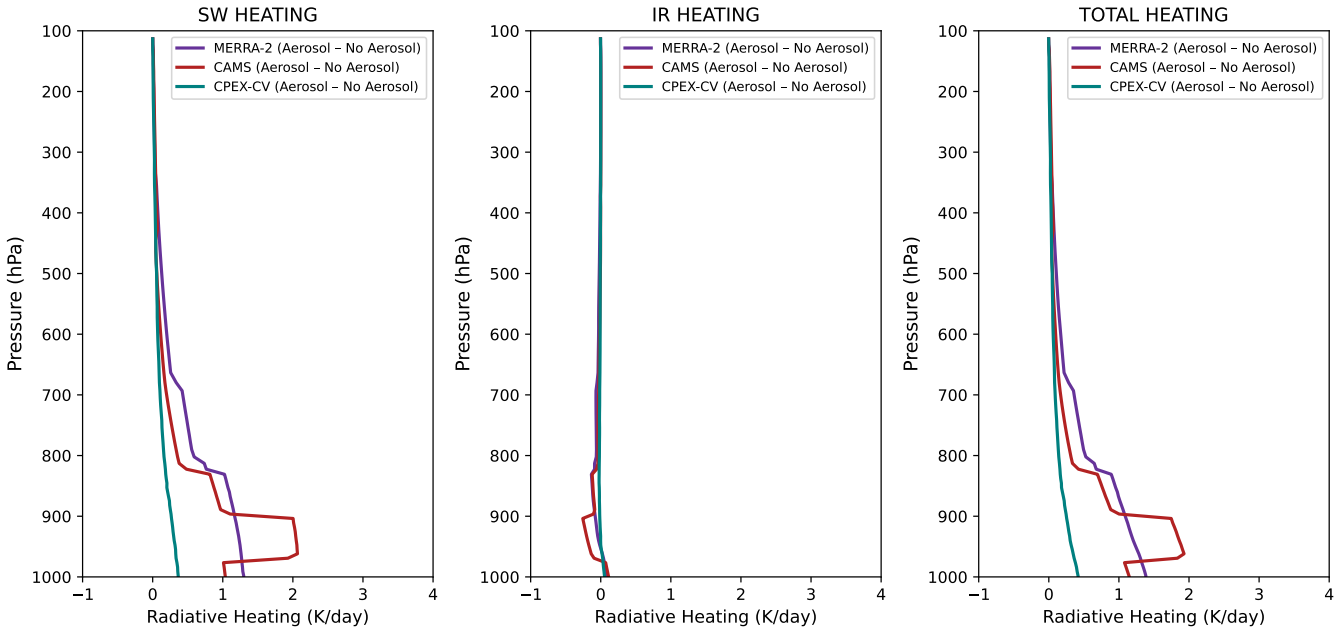

Figure 4. Heating rate difference between aerosol-aware and control run for MERRA-2 (purple), CAMS (red) and CPEX-CV (teal) for the background dust case. The left panel shows SW heating, the center panel shows LW/IR heating and the right panel shows total heating.

processes rather than IR. The fact that most CPEX-CV sampling occurred during the morning and close to solar noon may explain some of this behavior, but it is not the sole factor and ~~could~~ can also be attributed to the choice of optical properties within the FLG RTM. Saharan dust, often composed of mineral-rich particles, ~~can both absorb and scatter incoming sunlight~~is very active in the SW. Consequently, the presence of Saharan dust in the atmosphere leads to the absorption of a significant portion of SW radiation, resulting in the localized heating effects we ~~observed in the differential of heating rates .~~ observe in the heating rates differential.

The marginal disparity observed between aerosol and ~~no-aerosol runs in SW~~ control runs in the LW/IR radiation can be ~~attributed to~~ explained by the inherent characteristics of the optical properties for transported dust within ~~FLG, particularly their relatively subdued impact in the SW spectral region.~~ the model. Unlike certain aerosols such as sulfates and nitrates that highly influence LW/IR radiation, mineral dust aerosols, including those from Saharan dust, tend to exhibit lower absorption efficiency in the LW/IR spectrum. Their contribution to LW/IR radiative forcing is further limited by ~~a~~ the dominance of scattering effects in SW radiation, where dust aerosols are more influential. Additionally, the intricate interplay of various radiative forcing components, including water vapor and greenhouse gases, may overshadow the specific impact of dust aerosols in the LW/IR region. The size, composition, and altitude of dust particles also play roles in determining their radiative properties.

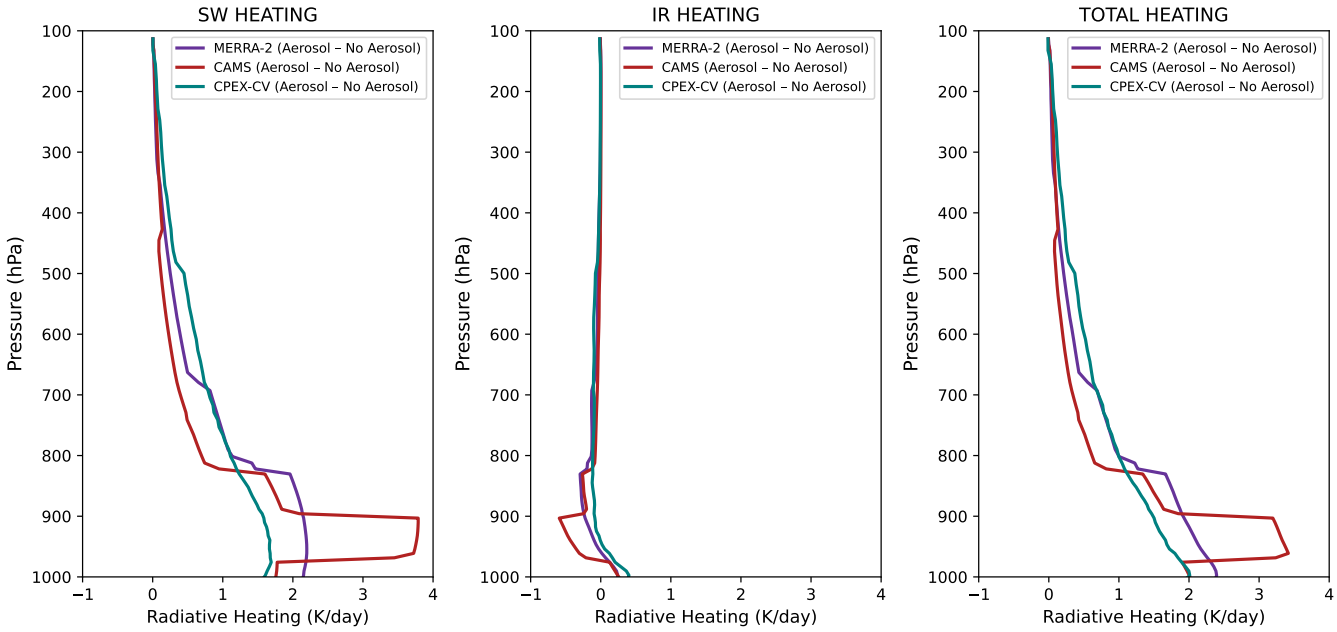

Figure 5. Heating rate difference between aerosol-aware and control run for MERRA-2 (purple), CAMS (red) and CPEX-CV (teal) for the anomalous dust case. The left panel shows SW heating, the center panel shows LW/IR heating and the right panel shows total heating.

Figure 5 ~~is similar to~~ displays the same calculation as Fig. 4 but ~~focuses on~~ for heating rates calculated for anomalous dust profiles with AOD exceeding 0.335 as defined previously. The impact of anomalous dust on heating rates is evident when compared with Fig. 4; higher AOD values correspond to higher heating rates. ~~However, notable differences~~ The MERRA-2 SW heating difference reaches up to 2.2 K/day, while the CAMS SW heating rate difference reaches up to 3.8 K/day. Notable differences with Fig. 4 are observed in the reanalysis data, ~~with significantly higher heating rates~~ where heating rates are higher than those calculated from CPEX-CV data below 800 hPa ~~and smaller rates (compared to calculations using observed data) between 800 and 400 hPa. Additionally, there is an~~ but lower than those calculated from CPEX-CV data between 700 and 250 hPa. The differences between reanalysis and CPEX-CV heating rates are shown in Fig. 5 and 6 and discussed in the next section. There is also a notable increase in LW/IR cooling below 800 hPa ~~, particularly in~~ in both MERRA-2 and CAMS in comparison with the findings in Fig. 4

~~Heating rate difference between aerosol-aware and control run for MERRA-2 (purple), CAMS (red) and CPEX-CV (teal) for the anomalous dust case. The left panel shows SW heating, the center panel shows LW/IR heating and the right panel shows total heating.~~

~~The marginal disparity observed between aerosol and no-aerosol runs in the~~ , and an increase in LW/IR ~~radiation can be explained by the inherent characteristics of the optical properties for transported dust within the model. Dust aerosols have a relatively subdued impact in the LW/IR spectral region, meaning they are less effective at absorbing and re-emitting LW/IR~~

radiation compared to other aerosols that might be more influential in this spectrum. heating in the surface levels. However, the total heating remains driven by the SW heating.

3.3 Dataset comparison

The impact of assimilating CPEX-CV data into the MERRA-2 reanalysis was assessed by comparing it differencing MERRA-2 heating rates with CPEX-CV profiles heating rates considered as the truth. This difference in heating rate is contrasted with the difference between CAMS heating rates and truth (CPEX-CV), because CAMS did not assimilate CPEX-CV data. This comparison of reanalysis minus truth sheds light on the performance of MERRA-2 in accurately representing aerosol-induced heating rates after the assimilation of high vertical resolution aerosol extinction coefficient profiles. The differences between the reanalysis and truth were examined for both aerosol-aware runs and control runs, specifically focusing on focusing on both background and anomalous dust concentrations. In Fig. 6, the differences for background AOD (AOD < 0.2) are depicted, while Fig. 7 illustrates the differences for anomalous AOD. In both figures, the purple line represents the heating rate difference between MERRA-2 and CPEX-CV (MERRA-2 minus CPEX-CV), and the red line represents the heating rate difference between MERRA-2 and CAMS (MERRA-2 minus CAMS CAMS and CPEX-CV (CAMS minus CPEX-CV). The solid lines correspond to the aerosol-aware run, while the dotted lines represent the control run.

Examining the MERRA-2 background AOD case in Fig. 6, the difference in SW heating below 700 hPa is nearly 0 reaches 0.9 K/day for the control case, increasing to around 0.7 K/day at the surface in the aerosol-aware run . For anomalous dust concentrations in Fig. 7, aerosol-aware runs exhibit similar differences in SW heating for MERRA-2 below 800 hPa. Regarding LW/IR heating , substantial (solid purple line), and drops significantly around 825 hPa. The largest dust-induced SW heating differences between MERRA-2 and truth, reaching up to 1.7 K/day between 700 hPa and 500 hPa, are evident for both aerosol-aware and control runs. In the background dust case (Fig. 6), these CPEX-CV are thus at these lower levels of the atmosphere. Strong differences in LW/IR heating are more pronounced, exceeding 2 seen for MERRA-2, exceeding 1.55 K/day around 600 hPa. Smaller differences in The control run LW/IR heating are observed for anomalous AOD cases, reaching nearly 1.5 Kprofiles are very similar to the aerosol-aware profiles, highlighting the lack of LW/day around 700 hPa IR interaction of dust with LW/IR radiation. For anomalous dust concentrations in Fig. 7. Importantly, these significant differences in heating rates persist at crucial atmospheric levels despite the assimilation of CPEX-CV data into 7, the aerosol-aware run exhibits a similar SW heating profile to the background dust profile in Fig. 6 for MERRA-2 . below 825 hPa, with a maximum of 0.6 K/day at the surface. This suggests that MERRA-2 represents the truth better at higher dust concentrations. The LW/IR heating profile exhibits similar differences to the background dust case depicted in Fig. 6, consistent with the fact that dust does not interact strongly with LW/IR radiation.

For both background AOD and anomalous AOD cases, as shown in Fig. 6 and 7, the SW heating difference between CAMS and truth is almost 0 around 1.7 K/day for SW heating below 700 hPa in the control run. Notably, an increase of up to 1.5 K/day between 975 hPa and 900 hPa is observed in the aerosol-aware run for the background AOD case, and up to 2.2 2.05 K/day for anomalous dust cases. This discrepancy suggests a potential misplacement of a dust layer by the reanalysis is mainly driven by the CAMS humidity profile at this atmospheric level. Differences Large discrepancies in LW/IR between CAMS

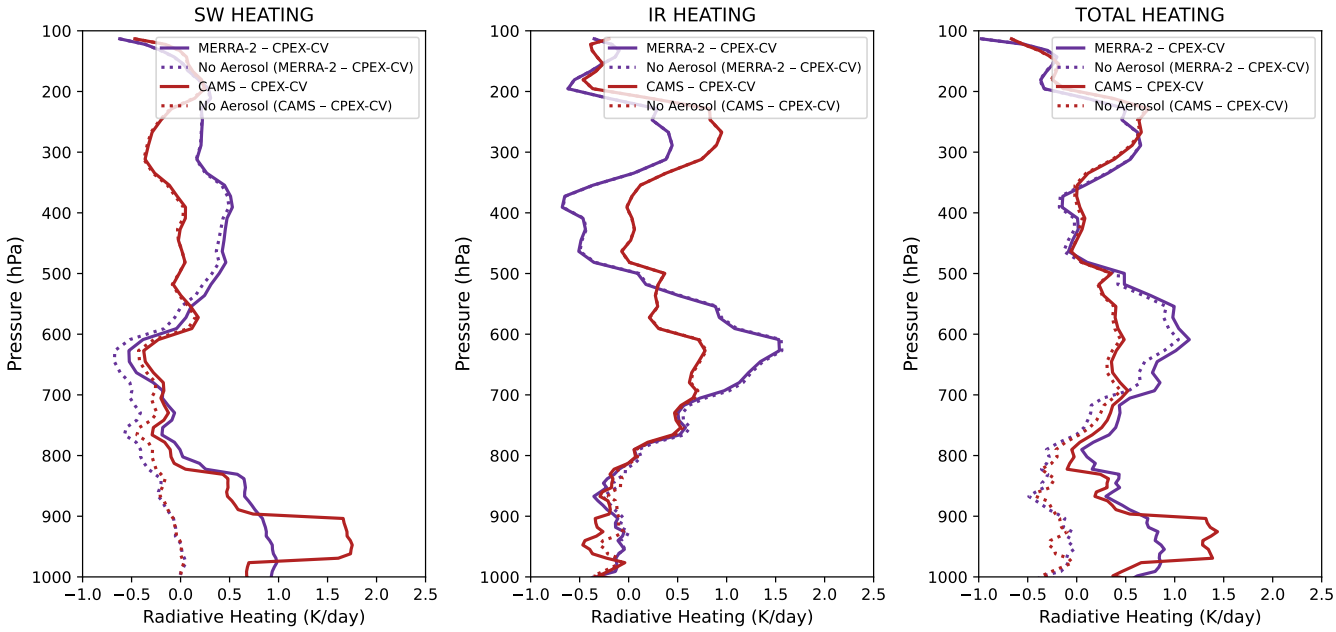

Figure 6. Heating rate difference between reanalysis and observation for the background dust case. Differences between MERRA-2 and CPEX-CV are plotted in purple and differences between CAMS and CPEX-CV are plotted in red. The solid lines correspond to the aerosol-aware run and the dotted lines correspond to the control run.

and truth are evident between 700 hPa and 500 hPa for both aerosol-aware and control runs, reaching up to ~~0.8~~ 0.75 K/day for ~~both~~ background AOD and 1.2 K/day for anomalous AOD cases. ~~Notably, these differences are smaller~~ The LW/IR heating difference between CAMS and truth is smaller between 700 hPa and 550 hPa than those observed between MERRA-2 and truth, ~~highlighting the persistent challenges even with MERRA-2's~~ but is larger above 500 hPa. However, these differences are not likely driven by errors in dust aerosol characterization since there are minimal differences between the control run and the aerosol-aware run.

A major result from Fig. 6 and 7. is that despite the assimilation of CPEX-CV ~~data.~~ HALO aerosol profiles into the MERRA-2 reanalysis dataset, large errors in SW rates persist throughout the atmosphere between MERRA-2 and what was observed during CPEX-CV. The average aerosol-aware MERRA-2 SW heating difference with CPEX-CV is 0.37 K/day, and the average aerosol-aware CAMS SW heating difference with CPEX-CV is 0.54 K/day. While MERRA-2 performs better than CAMS at representing truth, heating rate differences of the magnitude shown in these figures have a non-negligible effect on the atmosphere and cannot be ignored in modeling without repercussions on outputs.

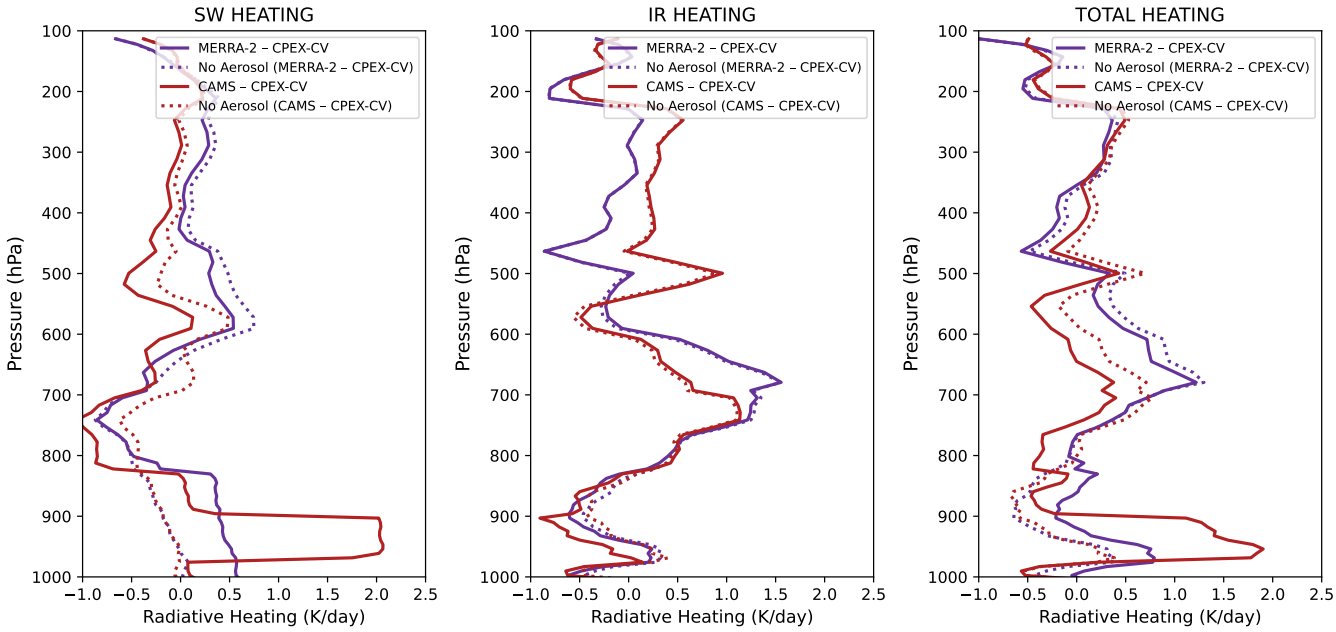

Figure 7. Heating rate difference between reanalysis and observation for the anomalous dust case. Differences between MERRA-2 and CPEX-CV are plotted in purple and differences between CAMS and CPEX-CV are plotted in red. The solid lines correspond to the aerosol-aware run and the dotted lines correspond to the control run.

3.4 Comparison with an extreme dust event: The June 2020 Godzilla dust storm

To elucidate the distinctions in aerosol representation and subsequent impacts on heating rates between the MERRA-2 and CAMS reanalyses, specifically in the absence of cloud-related influences as encountered in the context of AEWs, we conducted a comparative analysis. This investigation focused on a notable event known as the Godzilla dust storm, an extreme dust-only occurrence in June 2020 within the same geographic region. Notably documented in the literature (Yu et al., 2021), the event showcased unprecedented AOD levels, as depicted in Fig. 8 for 18 June ~~.~~2020. The FLG RTM was employed to compute heating rates for a profile situated at 15°N and 20°W at 12:00Z, corresponding to an AOD of 2.70. The resultant aerosol impact, as illustrated in Fig. 9, accentuates the increase in SW heating profiles. CAMS exhibits pronounced SW heating concentrated between 950 hPa and 900 hPa, while MERRA-2 displays lower peak values but a broader range extending from the surface to around 800 hPa. ~~Interestingly, the~~ The LW/IR heating differences ~~hover~~ are a few degrees above 0 K/day at the surface levels and remain close to 0 K/day day at higher levels for both MERRA-2 and CAMS. These findings align consistently with our prior analysis conducted in September 2022, reinforcing the robustness of the observed profiles and the utility of the FLG RTM in capturing the nuances of aerosol-induced heating variations outside of cloud-influenced scenarios associated with AEWs.

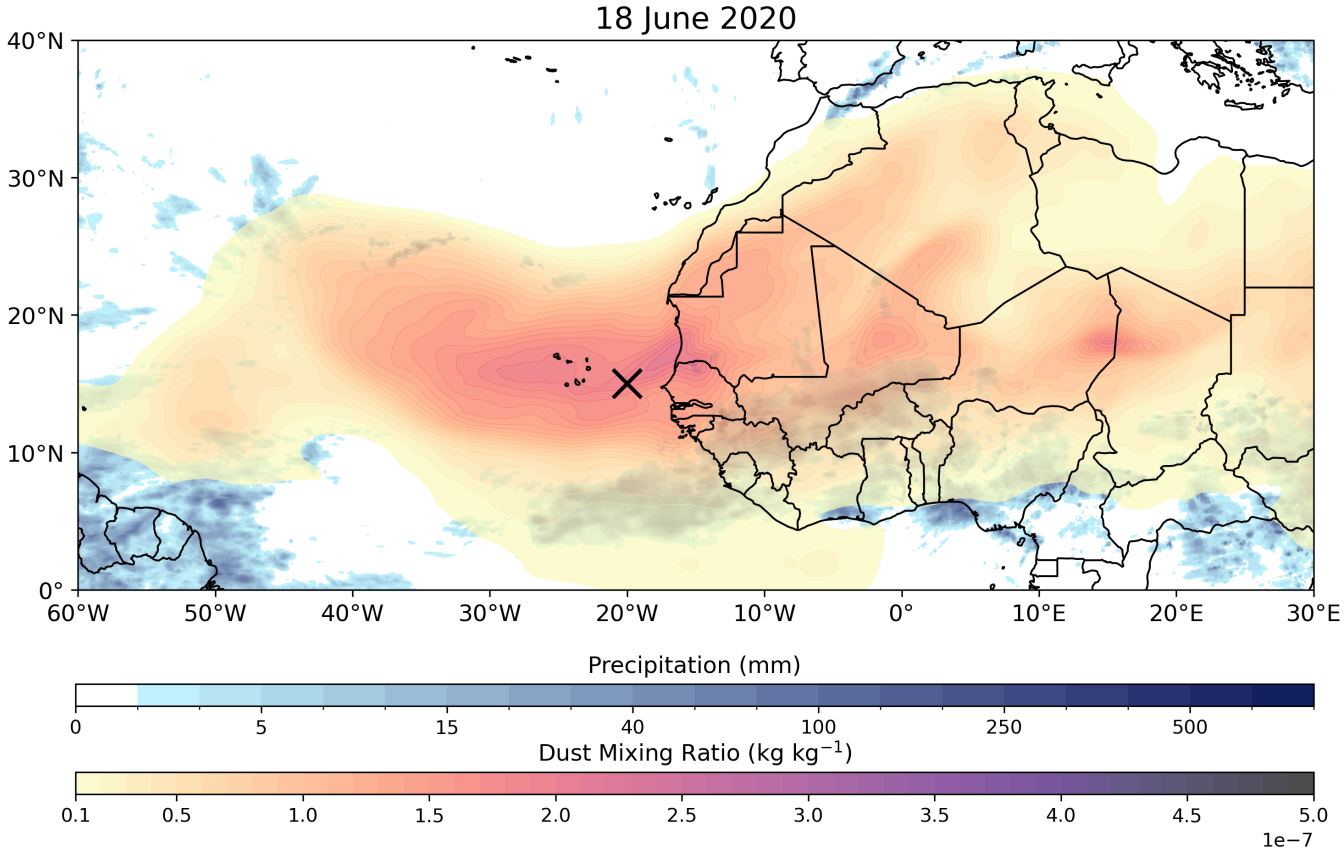

Figure 8. MERRA-2 total dust mixing ratio and IMERG daily accumulated precipitation on 18 June 2020. The location of the profile used in the analysis is marked in black.

3.5 Case study: Hurricane Fiona and TS Hermine

We analyze the effect of aerosol on heating rates ~~for~~ using all three datasets on two days of interest (9 September 2022 and 22 September 2022) ~~, using mean profiles of pressure, temperature, specific humidity, and extinction from HALO averaged over the flight path~~in the context of developing AEWs. The RTM simulations are performed after ~~taking into consideration~~ accounting for the solar zenith angle at the mean local time and location of the flight. The research flight on 09 September flew through AEW 4, which later developed into Hurricane Fiona. The research flight on 22 September flew through AEW 8, which soon after developed into TS Hermine. Table 4 shows the mean, maximum, and standard deviation of AOD on both days studied as measured by the three datasets used in the case study, where the MERRA-2 and CAMS values are calculated from the collocation with the CPEX-CV flight path. The mean AOD was higher for the three datasets on 22 September 2022 than on 09 September, and this difference in the CPEX-CV dataset is nearly two times larger than the difference between the two days

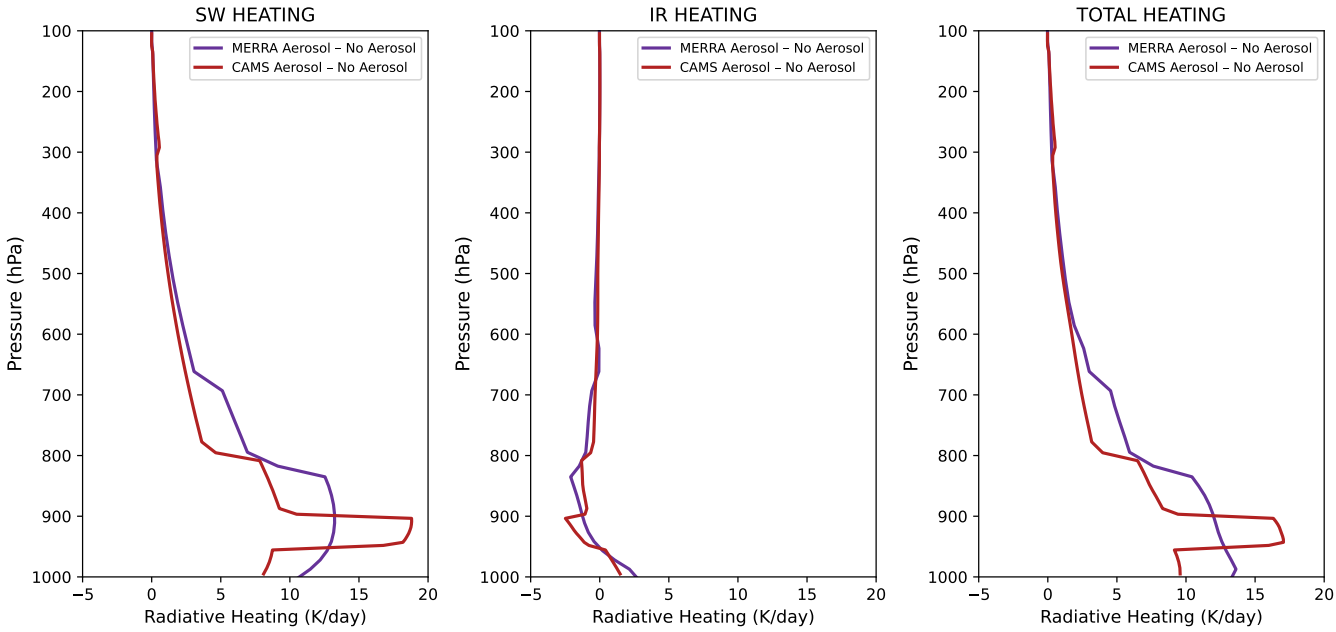

Figure 9. Heating rate difference between aerosol-aware and control run for MERRA-2 (purple) and CAMS (red) at 15°N, 20°W on 18 June 2020. The left panel shows SW heating, the center panel shows LW/IR heating and the right panel shows total heating.

Table 4. Mean, maximum and standard deviation of AOD for CPEX-CV, MERRA-2 and CAMS on 09 and 22 September 2022.

	09 September 2022			22 September 2022		
Dataset	Mean AOD	Maximum AOD	Standard Deviation	Mean AOD	Maximum AOD	Standard Deviation
CPEX-CV	0.25	1.69	0.16	1.02	3.34	0.64
MERRA-2	0.33	0.72	0.16	0.59	2.49	0.48
CAMS	0.32	0.69	0.17	0.59	1.30	0.34

in the reanalysis datasets. Of note is also the maximum AOD of 3.34 captured by CPEX-CV, which is significantly larger than the maximum AOD in the MERRA-2 dataset (2.49) and the CAMS dataset (1.30).

Figure 10 illustrates the difference in aerosol mean heating rates between the aerosol-aware and control runs during the research flight on 09 September, where the average AOD value was 0.25 according to the CPEX-CV dataset. The greatest
435 difference between CPEX-CV and reanalysis datasets are once again seen in the SW heating profile. Figure 10 shows a SW heating of ~~nearly~~ 1 K/day at the surface which decreases with height for the CPEX-CV dataset. ~~This~~ Consistent with our analysis above, this SW heating rate is greatly overestimated by both the MERRA-2 and CAMS reanalyses, with a heating rate

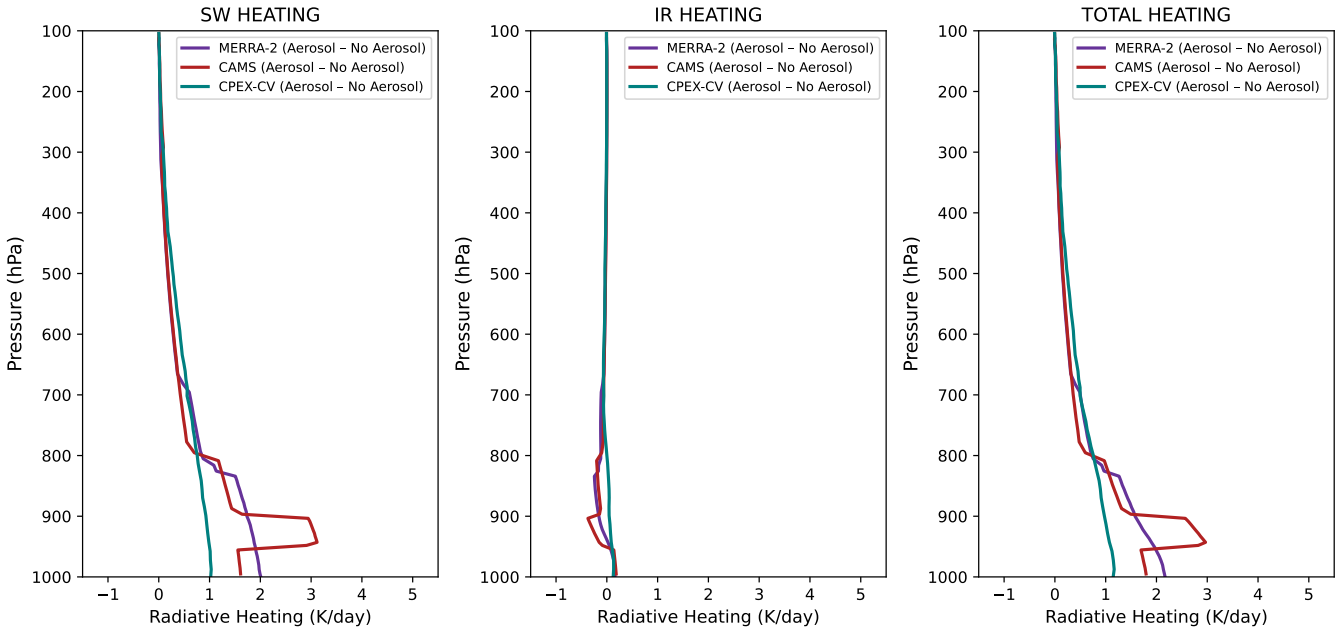

Figure 10. Heating rate difference between aerosol-aware and control run for MERRA-2 (purple), CAMS (red) and CPEX-CV (teal) on 09 September 2022. The left panel shows SW heating, the center panel shows LW/IR heating and the right panel shows total heating.

of 2 K/day at the surface for MERRA-2 and a heating rate of ~~over 1.5~~ 1.6 K/day at the surface for CAMS, reaching up to 3 K/day between 950 hPa and 900 hPa.

Figure 11 ~~illustrates the difference~~ shows striking differences in aerosol mean heating rates between the aerosol-aware and control run during the research flight on 22 September, where the average AOD value was 1.02~~. This~~ , over 4 times larger than on 09 September 2022. The CPEX-CV dataset shows a SW heating of ~~nearly 2~~ 1.9 K/day at the surface~~which stays around this value~~ , remaining between 1.9 K/day and 2.4 K/day up to 700 hPa~~and then decreases with height for the CPEX-CV dataset~~, and decreasing with height above 800 hPa. This SW heating rate is once again overestimated by ~~both~~ the MERRA-2 reanalysis below 800 hPa, with a heating rate of ~~around~~ 2.3 K/day at the surface~~for MERRA-2 and a heating rate~~. The SW heating rate at the surface from CAMS is ~~similar~~ nearly identical to the heating rate from CPEX-CV, but the same increase in SW heating for CAMS between 950 hPa and 900 hPa ~~reaches nearly 4.5~~ attributed to the humidity profile as seen in previous cases reaches 4.4 K/day. Above 800 hPa, the two reanalyses greatly underestimate the SW heating rate in this case, with differences of over 1 K/day between CPEX-CV and reanalysis. The CPEX-CV data reveals that the heating is evenly distributed throughout the column, whereas the reanalyses overestimate heating at the lower levels and underestimate heating at the upper levels. These differences in the structure of vertical heating will likely impact the forecast of the development of AEWs. High dust concentration has the potential to strongly alter the heating profile, as illustrated in Fig. 11, exacerbating differences between reanalysis and observation. In the context of developing AEWs, the heating rate differences between

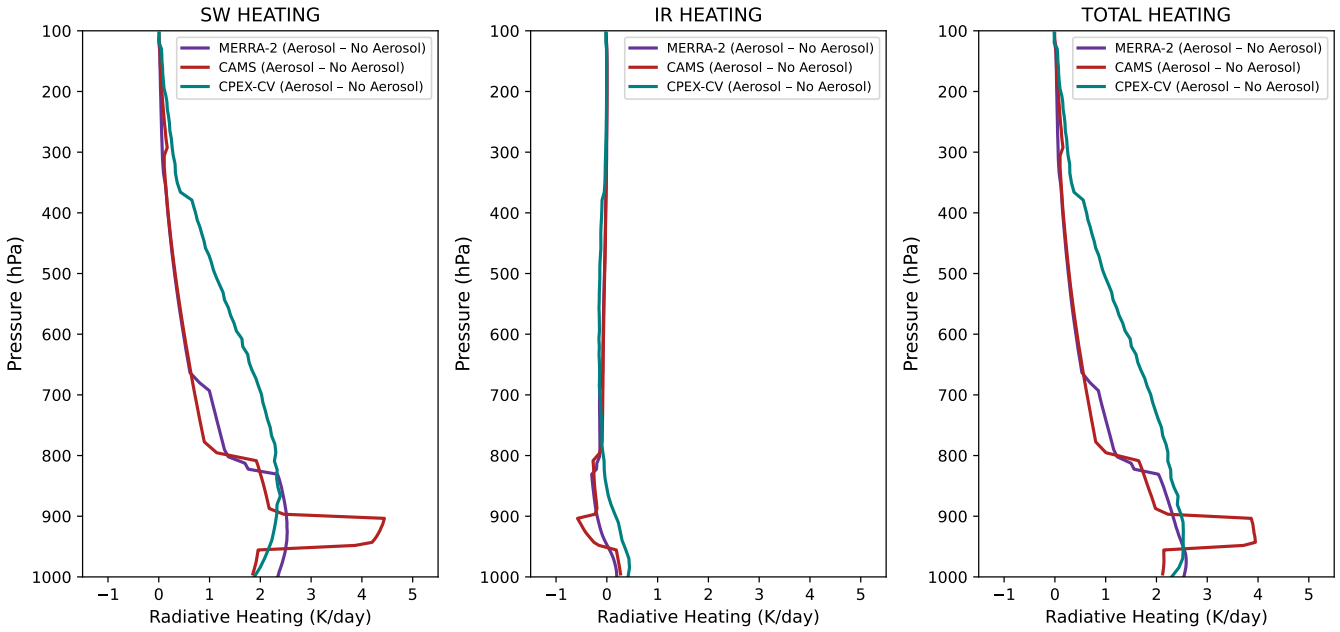

Figure 11. Heating rate difference between aerosol-aware and control run for MERRA-2 (purple), CAMS (red) and CPEX-CV (teal) on 22 September 2022. The left panel shows SW heating, the center panel shows LW/IR heating and the right panel shows total heating.

observation (CPEX-CV) and reanalysis represent a significant inadequacy in atmospheric characterization, which must be addressed to avoid repercussions on model outputs of such systems. Furthermore, Table 4 indicates the differences in AOD between CPEX-CV and reanalysis datasets are even greater at some locations, where CPEX-CV captured AOD values of up to 3.34, meaning that the differences captured in the mean heating rate profile in Fig. 11 may be even larger at specific profile locations.

We analyze the structure of the dust-induced shortwave heating throughout the progression of Fiona and Hermine. We use the AEW tracker documented in Lawton et al. (2022) to collocate MERRA-2 and CAMS profiles with the center of the storm, and calculate dust-induced (aerosol-aware minus control) SW heating rates. As shown previously, the dust-induced total heating rates are driven primarily by SW radiation. Because there is no SW activity during nighttime only daytime profiles are studied. The profiles shown in Fig. 12 correspond to profiles at the closest gridpoint to the center of the storm as determined by the AEW tracker. The first profile corresponds to the first time-step where the center of the developing AEW was located over the ocean rather than land. The heating rate evolution is plotted for the peak moments of the storms: the last profile for Fiona corresponds to the last time-step before the storm made landfall and subsequently weakened, whereas the last profile for Hermine corresponds to the last time-step before the storm became a post-tropical remnant low. Figure 12 reveals important differences between the dust-induced SW heating during Fiona's development in comparison to Hermine's. Based on the previous comparisons of heating rates calculated from reanalysis against those from observational data, we have determined

that the MERRA-2 dataset captures the most accurate representation of the vertical structure of heating of the two reanalyses. In Fig. 12, MERRA-2 shows that the heating below 800 hPa varies between values of 0.52 K and 1.59 K/day throughout the development of Fiona. On the other hand, heating at 12 UTC on 23 and 24 September 2022 reaches up to 2.78 K/day. This large difference in SW heating is noteworthy in the context of the short lifespan of Hermine, which was unable to intensify to the scale of Fiona (Category 4 Hurricane). The high degree of heating in the last profile for Fiona can be attributed to an anomalously high AOD value (0.64), while in previous time steps, AOD remained between 0.07 and 0.20. The max AOD value for the profiles plotted during Hermine was 0.4. The CAMS profiles show similar results to the MERRA-2 dataset, but still overestimate the SW heating around 900 hPa. The heating at 12 UTC on 24 September 2022 is also much lower for CAMS with a peak heating value of 1.34 K/day versus 2.64 K/day for MERRA-2.

Over the ocean, dust tends to reduce specific humidity in the lower troposphere, particularly in regions with high aerosol loading, while simultaneously augmenting midlevel moisture levels. Dust also warms the lower troposphere, promoting convection and generating positive vorticity between approximately 800–1,000 hPa (Sun and Zhao, 2020; Xian et al., 2020), where most of the aforementioned SW induced heating rates in both reanalysis prevail. This warming effect can also enhance vertical wind shear. Consequently, this impacts environmental conditions in tropical cyclone genesis regions. While we recognize this is not enough to draw a conclusion, since microphysics are not considered, and isolating the impact of thermodynamics to just aerosols is difficult, we believe it is an important consideration.

3.6 A note on clouds

It is crucial to emphasize that our investigation, utilizing CPEX-CV data and the Godzilla dust storm event, provides valuable insights into aerosol-induced heating variations. Radiation calculations primarily rely on dust fields and include parameters such as pressure, temperature, moisture, and ozone profiles. The model acknowledges clouds based on moisture profiles but does not explicitly represent critical factors such as liquid water path and specific optical properties associated with clouds. This recognition highlights the limited scope of the cloud-related information provided by the model, underscoring the necessity for future research to integrate a more comprehensive treatment of cloud-related variables for a detailed understanding of atmospheric interactions.

4 Conclusions

The paper explores the ~~intricate interactions between African Easterly Waves (AEWs) and Saharan dust~~ impact of Saharan dust plumes on atmospheric heating rates in the context of African Easterly Wave (AEW) development using radiative examination techniques based on reanalysis and NASA airborne observations. The study leverages data from the Convective Processes Experiment – Cabo Verde (CPEX-CV) and multiple reanalysis datasets, including MERRA-2 and CAMS. The study examined data from seven DC-8 flights during the CPEX-CV field campaign, corresponding to 10 different AEWs, with a special emphasis on four waves that developed into named tropical storms, ~~and two of them~~ two intensifying into hurricanes. The primary objectives include assessing the accuracy of reanalysis in depicting aerosol radiative properties, ~~understanding~~

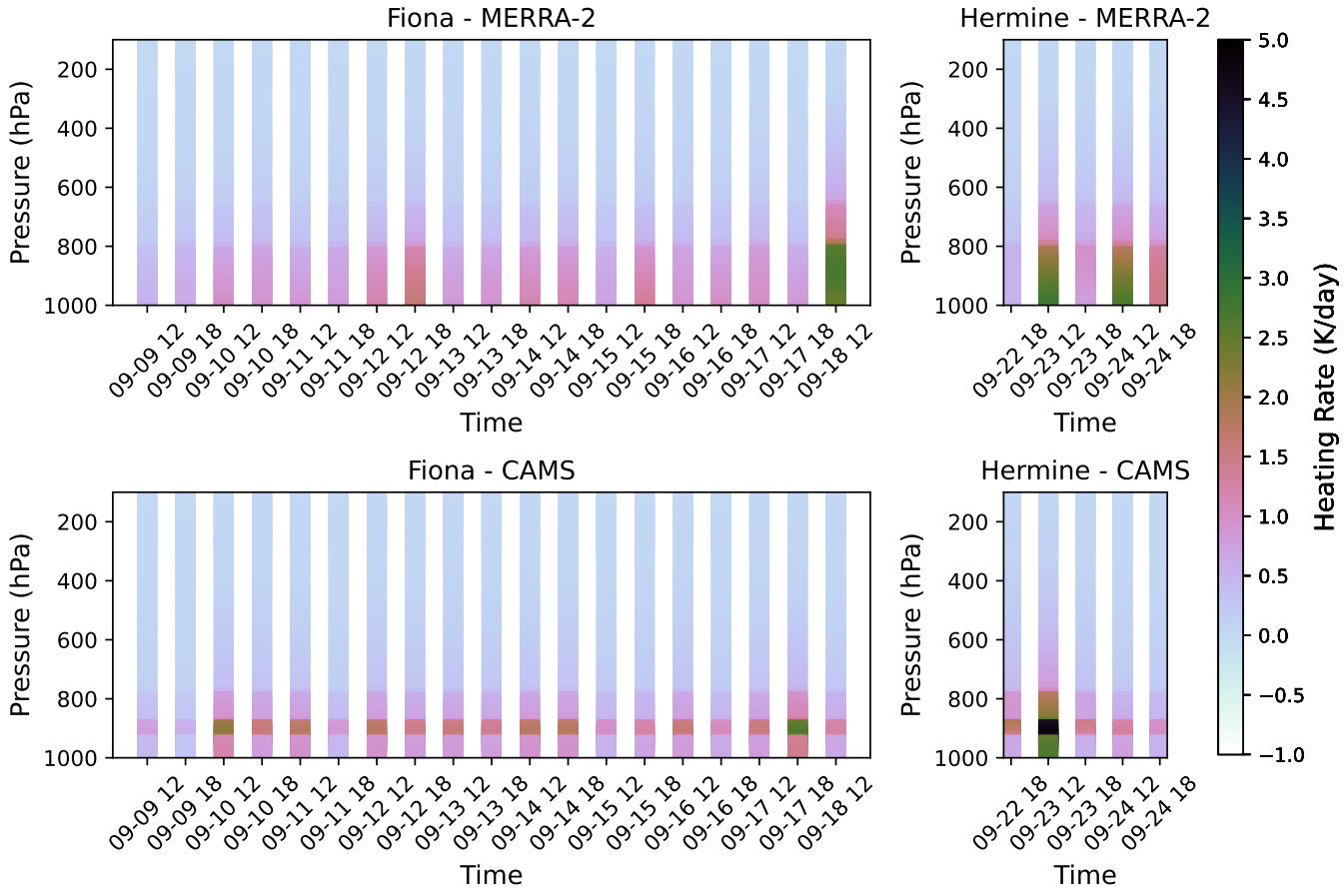

Figure 12. Vertical profiles of heating rates (K/day) at the center of two developing AEWs following their development into named storms (Fiona, left and Hermine, right) for two reanalysis datasets (MERRA-2, top and CAMS, bottom).

~~the influence of aerosol heating rates, especially from Saharan dust , on AEW development~~comparing the impact of Saharan dust on atmospheric heating rates in different AEW scenarios, and evaluating the impact of aerosol assimilation on model representation. The methodology integrates observational data from CPEX-CV with a four-stream radiative transfer model (Fu-Liou-Gu RTM), utilizing aerosol profiles from MERRA-2 and CAMS reanalyses.

The research revealed significant variations in aerosol-induced heating rates between ~~observed data and reanalyses,~~ observational data (CEPX-CV) and reanalyses (MERRA-2 and CAMS~~as compared with heating rates calculated with the observational data collected over CPEX-CV~~). The reanalyses exhibited significant differences in extinction and atmospheric profiles compared to observed data, impacting the calculation of total heating rates. Both MERRA-2 and CAMS radiative transfer runs consistently overestimated shortwave (SW) heating rates below 800 hPa, with errors up to 2.05 K for the CAMS dataset in anomalous dust cases, and errors up to 0.6 K for MERRA-2 even after assimilating CPEX-CV data~~(which is the case for MERRA-2)~~.

This was due to notable disparities in the representation of aerosol in extinction coefficient and aerosol optical depth (AOD). MERRA-2 exhibited higher surface extinction ~~but missed~~ coefficient than what was measured by CPEX-CV at the surface but missed the variability throughout the tropospheric column that was captured by ~~observational data. On the other hand, CAMS consistently underestimated aerosol extinction compared to the~~ the observational data, revealing challenges in accurately representing aerosol effects in models. Errors in CAMS humidity and extinction profiles resulted in an overestimation of heating below 900 hPa. Both reanalyses also ~~had too much AOD~~ exhibited too high AOD values in background cases as contrasted with CPEX-CV data ~~or too little~~ and too low values in the anomalous cases. A comparative analysis of an extreme dust event (June 2020 Godzilla dust storm) reinforced the findings, showcasing differences of over 5K in SW heating profiles between MERRA-2 and CAMS. This analysis provided further evidence of the robustness of observed profiles and the model's ability to capture aerosol-induced heating variations. Finally, ~~case studies~~ a case study focusing on Hurricane Fiona and Tropical Storm Hermine illustrated the impact of aerosols on heating rates during specific research flights. Both reanalyses exhibited notable discrepancies in SW heating rates compared to observed data, with potential implications for forecasting the development of AEWs.

When considering the impact of heating rates on tropical cyclone development, a noteworthy observation emerges regarding the impact of varying dust concentrations on the process, particularly in relation to heating rates. The ~~distinction between anomalous and background dust cases introduces a fascinating dynamic, unveiling a correlation between lower dust levels during the AEW development~~ difference in the vertical heating profile between lower (AOD = 0.25) and higher (AOD = 1.02) dust concentrations as revealed on 09 and ~~the formation of exceptionally potent hurricanes (in the cases of Ian and Fiona)~~22 September 2022 highlights the potential existence of a dust concentration threshold over which dust-induced atmospheric heating acts to affect the development of the system. Dust concentration and thus dust-induced radiative heating during the sampling of Pre-Fiona, which intensified to a Category 4 hurricane, was significantly lower than during the sampling of Hermine. Strikingly, when Hurricane Hermine was sampled, characterized by elevated dust concentrations and higher dust-induced heating rates, the storm exhibited a subsequent weakening and a ~~short lived~~ short-lived time span. Of course, it is essential to acknowledge that this analysis represents a gross simplification of a complex system, and a more comprehensive examination of environmental factors is imperative for a nuanced understanding. Despite this oversimplification, the observed patterns underscore the significance of incorporating dust-related variables in hurricane modeling studies. Following the progression heating rate profiles throughout the storm, we notice significantly lower heating rates (0.52 K/day to 1.59 K/day) during Fiona's development than during Hermine (up to 2.78 K/day). This warrants a more in-depth investigation to elucidate the intricate interplay between dust concentrations, heating rates, and their influence on hurricane development, emphasizing the necessity for rigorous modeling studies to advance our comprehension of these intricate atmospheric phenomena. Furthermore, the vertical structure of the heating was inaccurately represented by the reanalyses, specifically in the case of Hermine, where heating was overestimated below 800 hPa but underestimated above 800 hPa, the CPEX-CV dataset revealing a much more uniform heating distribution than the two reanalyses. Such errors in the heating profile are likely to impact the modeling of the AEW development.

The research significantly advances our understanding of the ~~complex interactions between AEWs and Saharan dust, shedding light on the role of~~ importance of accurately characterizing aerosol-induced heating rates ~~in weather systems~~during AEW development. The findings underscore the limitations of current reanalysis datasets in accurately capturing aerosol properties and their radiative effects, particularly ~~in~~ at critical atmospheric levels (1000-500 hPa). Despite the assimilation of observational data, substantial differences persist, revealing the need for further refinement in modeling aerosol dynamics. The study emphasizes the importance of considering vertical distribution and composition of aerosols in assessing their impact on AEWs. ~~The~~ Unveiled by advanced radiative transfer modeling, the observed discrepancies in heating rates between reanalysis and airborne observations at key atmospheric levels have implications for weather forecasting, emphasizing the need for improved aerosol parameterizations in NWP models~~. The comprehensive approach, combining airborne observations with advanced radiative transfer modeling, provides~~ , and provide valuable insights into the challenges and opportunities for refining our understanding of ~~aerosol-climate~~ aerosol-AEW interactions in the Atlantic basin.

Data availability. The CPEX-CV data used in this study can be obtained from https://www-air.larc.nasa.gov/missions/cpex-cv/index.html (CPEX-CV, 2022). The MERRA-2 reanalysis data and surface parameters are available via NASA's Global Modeling and Assimilation Office website: https://gmao.gsfc.nasa.gov/reanalysis/MERRA-2/ and or via the NASA Goddard Earth Sciences (GES) Data and Information Services Center (DISC). The CAMS reanalysis can be found in https://atmosphere.copernicus.eu/data. Likewise, the Fu Liou Gu Radiative Transfer model code is available via the UCLA (http://people.atmos.ucla.edu/gu/Fu-Liou-Gu_Radiative_Transfer_Model.htm).

Author contributions. RWB led the radiative transfer study. RWB and MIOM designed the experiments. RWB was responsible for obtaining datasets used as input for the radiative transfer calculations. RWB conducted the radiative transfer modeling and performed the majority of the analysis and was supervised and assisted by MIOM. RWB and MIOM prepared the manuscript and figures.

Competing interests. The authors declare that they have no conflict of interest.

Acknowledgements. Authors Ruby W. Burgess and Mayra I. Oyola-Merced acknowledge the CPEX-CV team for collecting the data and making it available to the community (https://www-air.larc.nasa.gov/cgi-bin/ArcView/cpex.2022), as well as Professors Angela Rowe, Tristan L'Ecuyer, and Daniel Vimont for their feedback in the research process. This work was performed at the University of Wisconsin-Madison. Support for this research was provided by the Office of the Vice Chancellor for Research and Graduate Education at the University of Wisconsin–Madison with funding from the Wisconsin Alumni Research Foundation.

References

Bauer, S. E. and Menon, S.: Aerosol direct, indirect, semidirect, and surface albedo effects from sector contributions based on the IPCC AR5 emissions for preindustrial and present-day conditions, Journal of Geophysical Research: Atmospheres, 117, 2012.

Bedka, K. M., Nehrir, A. R., Kavaya, M., Barton-Grimley, R., Beaubien, M., Carroll, B., Collins, J., Cooney, J., Emmitt, G. D., Greco, S., Kooi, S., Lee, T., Liu, Z., Rodier, S., and Skofronick-Jackson, G.: Airborne lidar observations of wind, water vapor, and aerosol profiles during the NASA Aeolus calibration and validation (Cal/Val) test flight campaign, Atmospheric Measurement Techniques, 14, 4305–4334, https://doi.org/10.5194/amt-14-4305-2021, 2021.

Buchard, V., Randles, C., Da Silva, A., Darmenov, A., Colarco, P., Govindaraju, R., Ferrare, R., Hair, J., Beyersdorf, A., Ziemba, L., et al.: The MERRA-2 aerosol reanalysis, 1980 onward. Part II: Evaluation and case studies, Journal of Climate, 30, 6851–6872, 2017.

Burpee, R. W.: The origin and structure of easterly waves in the lower troposphere of North Africa, Journal of the Atmospheric Sciences, 29, 77–90, 1972.

Carlson, T. N.: Some remarks on African disturbances and their progress over the tropical Atlantic, Monthly Weather Review, 97, 716–726, 1969.

Carlson, T. N. and Prospero, J. M.: The large-scale movement of Saharan air outbreaks over the northern equatorial Atlantic, Journal of Applied Meteorology and Climatology, 11, 283–297, 1972.

Carroll, B. J., Nehrir, A. R., Kooi, S. A., Collins, J. E., Barton-Grimley, R. A., Notari, A., Harper, D. B., and Lee, J.: Differential absorption lidar measurements of water vapor by the High Altitude Lidar Observatory (HALO): retrieval framework and first results, Atmospheric Measurement Techniques, 15, 605–626, 2022.

Dunion, J. P. and Velden, C. S.: The impact of the Saharan air layer on Atlantic tropical cyclone activity, Bulletin of the American Meteorological Society, 85, 353–366, 2004.

Fu, Q. and Liou, K.: On the correlated k-distribution method for radiative transfer in nonhomogeneous atmospheres, Journal of Atmospheric Sciences, 49, 2139–2156, 1992.

Fu, Q. and Liou, K. N.: Parameterization of the radiative properties of cirrus clouds, Journal of Atmospheric Sciences, 50, 2008–2025, 1993.

Fu, Q., Liou, K., Cribb, M., Charlock, T., and Grossman, A.: Multiple scattering parameterization in thermal infrared radiative transfer, Journal of the atmospheric sciences, 54, 2799–2812, 1997.

Gelaro, R., McCarty, W., Suárez, M. J., Todling, R., Molod, A., Takacs, L., Randles, C. A., Darmenov, A., Bosilovich, M. G., Reichle, R., et al.: The modern-era retrospective analysis for research and applications, version 2 (MERRA-2), Journal of climate, 30, 5419–5454, 2017.

GMAO: Supplemental Documentation for GEOS Aerosol Products, Tech. rep., NASA GMAO, 2023.

GOES-R Series Program: NOAA GOES-R Series Advanced Baseline Imager (ABI) Level 1b Data, NOAA National Centers for Environmental Information, https://doi.org/10.25921/tvws-w071, 2019.

Grogan, D. F. and Thorncroft, C. D.: The characteristics of African easterly waves coupled to Saharan mineral dust aerosols, Quarterly Journal of the Royal Meteorological Society, 145, 1130–1146, 2019.

Gu, Y., Liou, K., Ou, S., and Fovell, R.: Cirrus cloud simulations using WRF with improved radiation parameterization and increased vertical resolution, Journal of Geophysical Research: Atmospheres, 116, 2011.

Hess, M., Koepke, P., and Schult, I.: Optical properties of aerosols and clouds: The software package OPAC, Bulletin of the American meteorological society, 79, 831–844, 1998.

Hock, T. F., F. J. L.: The NCAR GPS Dropwindsonde, Bull. Amer. Meteor. Soc., 80, 407-420, 80, 407–420, 1999.

Huffman, G. J., Bolvin, D. T., Braithwaite, D., Hsu, K.-L., Joyce, R. J., Kidd, C., Nelkin, E. J., Sorooshian, S., Stocker, E. F., Tan, J., et al.: Integrated multi-satellite retrievals for the global precipitation measurement (GPM) mission (IMERG), Satellite Precipitation Measurement: Volume 1, pp. 343–353, 2020.

Inness, A., Ades, M., Agustí-Panareda, A., Barré, J., Benedictow, A., Blechschmidt, A.-M., Dominguez, J. J., Engelen, R., Eskes, H., Flemming, J., et al.: The CAMS reanalysis of atmospheric composition, Atmospheric Chemistry and Physics, 19, 3515–3556, 2019.

IPCC: Climate Change 2023: Synthesis Report. Contribution of Working Groups I, II and III to the Sixth Assessment Report of the Intergovernmental Panel on Climate Change [Core Writing Team, H. Lee and J. Romero (eds.)], IPCC, Geneva, Switzerland, 2023.

Jones, C., Mahowald, N., and Luo, C.: Observational evidence of African desert dust intensification of easterly waves, Geophysical research letters, 31, 2004.

Jury, M. R. and Santiago, M. J.: Composite analysis of dust impacts on African easterly waves in the Moderate Resolution Imaging Spectrometer era, Journal of Geophysical Research: Atmospheres, 115, 2010.

Karyampudi, V. M., Palm, S. P., Reagen, J. A., Fang, H., Grant, W. B., Hoff, R. M., Moulin, C., Pierce, H. F., Torres, O., Browell, E. V., et al.: Validation of the Saharan dust plume conceptual model using lidar, Meteosat, and ECMWF data, Bulletin of the American Meteorological Society, 80, 1045–1076, 1999.

Landsea, C. W., Bell, G. D., Gray, W. M., and Goldenberg, S. B.: The extremely active 1995 Atlantic hurricane season: Environmental conditions and verification of seasonal forecasts, Monthly Weather Review, 126, 1174–1193, 1998.

Lawton, Q. A., Majumdar, S. J., Dotterer, K., Thorncroft, C., and Schreck III, C. J.: The influence of convectively coupled Kelvin waves on African easterly waves in a wave-following framework, Monthly weather review, 150, 2055–2072, 2022.

Lei, L., Berkoff, T. A., Gronoff, G., Su, J., Nehrir, A. R., Wu, Y., Moshary, F., and Kuang, S.: Retrieval of UVB aerosol extinction profiles from the ground-based Langley Mobile Ozone Lidar (LMOL) system, Atmospheric Measurement Techniques, 15, 2465–2478, 2022.

Lenhardt, E. D., Gao, L., Redemann, J., Xu, F., Burton, S. P., Cairns, B., Chang, I., Ferrare, R. A., Hostetler, C. A., Saide, P. E., et al.: Use of lidar aerosol extinction and backscatter coefficients to estimate cloud condensation nuclei (CCN) concentrations in the southeast Atlantic, Atmospheric Measurement Techniques Discussions, 2022, 1–30, 2022.

Liou, K.-N., Fu, Q., and Ackerman, T. P.: A simple formulation of the delta-four-stream approximation for radiative transfer parameterizations, Journal of Atmospheric Sciences, 45, 1940–1948, 1988.

Lyapustin, A., Martonchik, J., Wang, Y., Laszlo, I., and Korkin, S.: Multiangle implementation of atmospheric correction (MAIAC): 1. Radiative transfer basis and look-up tables, Journal of Geophysical Research: Atmospheres, 116, 2011.

Ma, P.-L., Zhang, K., Shi, J. J., Matsui, T., and Arking, A.: Direct radiative effect of mineral dust on the development of African easterly waves in late summer, 2003–07, Journal of applied meteorology and climatology, 51, 2090–2104, 2012.

Mulcahy, J., Walters, D., Bellouin, N., and Milton, S.: Impacts of increasing the aerosol complexity in the Met Office global numerical weather prediction model, Atmospheric Chemistry and Physics, 14, 4749–4778, 2014.

Nalli, N. R. and Stowe, L. L.: Aerosol correction for remotely sensed sea surface temperatures from the National Oceanic and Atmospheric Administration advanced very high resolution radiometer, Journal of Geophysical Research: Oceans, 107, 36–1, 2002.

Nalli, N. R., Joseph, E., Morris, V. R., Barnet, C. D., Wolf, W. W., Wolfe, D., Minnett, P. J., Szczodrak, M., Izaguirre, M. A., Lumpkin, R., et al.: Multiyear observations of the tropical Atlantic atmosphere: Multidisciplinary applications of the NOAA Aerosols and Ocean Science Expeditions, Bulletin of the American Meteorological Society, 92, 765–789, 2011.

Nowottnick, E. P., Zawislak, J., Nehrir, A. R., Maring, H., Piña, A. J., McCarty, W., Reid, J. S., Chen, S.-H., Rowe, A. K., Sakaeda, N., et al.: The NASA Convective Processes Experiment-Cabo Verde (CPEX-CV): Mission Overview and Saharan Dust Measurements Obtained in the East Atlantic in September 2022, in: 103rd AMS Annual Meeting, AMS, 2023.

Oyola, M. I.: Implementation of a Global Dust Physical Sea Surface Temperature Retrieval For Numerical Weather Prediction Applications, Ph.D. thesis, Howard University, 2015.

Oyola, M. I., Campbell, J. R., Xian, P., Bucholtz, A., Ferrare, R. A., Burton, S. P., Kalashnikova, O., Ruston, B. C., and Lolli, S.: Quantifying the direct radiative effect of absorbing aerosols for numerical weather prediction: a case study, Atmospheric Chemistry and Physics, 19, 205–218, https://doi.org/10.5194/acp-19-205-2019, 2019.

Petty, G. W.: A First Course in Atmospheric Thermodynamics., Sundog Publishing, 2008.

Pratt, A. S. and Evans, J. L.: Potential impacts of the Saharan air layer on numerical model forecasts of North Atlantic tropical cyclogenesis, Weather and forecasting, 24, 420–435, 2009.

Ramanathan, V., Crutzen, P. J., Kiehl, J., and Rosenfeld, D.: Aerosols, climate, and the hydrological cycle, science, 294, 2119–2124, 2001.

Randles, C., Da Silva, A., Buchard, V., Colarco, P., Darmenov, A., Govindaraju, R., Smirnov, A., Holben, B., Ferrare, R., Hair, J., et al.: The MERRA-2 aerosol reanalysis, 1980 onward. Part I: System description and data assimilation evaluation, Journal of climate, 30, 6823–6850, 2017.

Reale, O., Lau, W. K., Kim, K.-M., and Brin, E.: Atlantic tropical cyclogenetic processes during SOP-3 NAMMA in the GEOS-5 global data assimilation and forecast system, Journal of the atmospheric sciences, 66, 3563–3578, 2009.

Reale, O., Lau, K., and da Silva, A.: Impact of interactive aerosol on the African easterly jet in the NASA GEOS-5 global forecasting system, Weather and forecasting, 26, 504–519, 2011.

Reed, R., Klinker, E., and Hollingsworth, A.: The structure and characteristics of African easterly wave disturbances as determined from the ECMWF operational analysis/forecast system, Meteorology and Atmospheric Physics, 38, 22–33, 1988.

Reed, R. J., Norquist, D. C., and Recker, E. E.: The structure and properties of African wave disturbances as observed during phase III of GATE, Monthly Weather Review, 105, 317–333, 1977.

Sun, Y. and Zhao, C.: Influence of Saharan dust on the large-scale meteorological environment for development of tropical cyclone over North Atlantic Ocean Basin, Journal of Geophysical Research: Atmospheres, 125, e2020JD033 454, 2020.

Thorncroft, C. and Blackburn, M.: Maintenance of the African easterly jet, Quarterly Journal of the Royal Meteorological Society, 125, 763–786, 1999.

Toll, V., Gleeson, E., Nielsen, K., Männik, A., Mašek, J., Rontu, L., and Post, P.: Impacts of the direct radiative effect of aerosols in numerical weather prediction over Europe using the ALADIN-HIRLAM NWP system, Atmospheric Research, 172, 163–173, 2016.

Xian, P., Klotzbach, P. J., Dunion, J. P., Janiga, M. A., Reid, J. S., Colarco, P. R., and Kipling, Z.: Revisiting the relationship between Atlantic dust and tropical cyclone activity using aerosol optical depth reanalyses: 2003–2018, Atmospheric Chemistry and Physics, 20, 15 357–15 378, 2020.

Xu, F., Van Harten, G., Diner, D. J., Kalashnikova, O. V., Seidel, F. C., Bruegge, C. J., and Dubovik, O.: Coupled retrieval of aerosol properties and land surface reflection using the Airborne Multiangle SpectroPolarimetric Imager, Journal of Geophysical Research: Atmospheres, 122, 7004–7026, 2017.

Yu, H., Tan, Q., Zhou, L., Zhou, Y., Bian, H., Chin, M., Ryder, C. L., Levy, R. C., Pradhan, Y., Shi, Y., et al.: Observation and modeling of the historic "Godzilla" African dust intrusion into the Caribbean Basin and the southern US in June 2020, Atmospheric Chemistry and Physics, 21, 12 359–12 383, 2021.

Zhang, J., Reid, J. S., Christensen, M., and Benedetti, A.: An evaluation of the impact of aerosol particles on weather forecasts from a biomass burning aerosol event over the Midwestern United States: observational-based analysis of surface temperature, Atmospheric Chemistry and Physics, 16, 6475–6494, 2016.